Meteorol. Atmos. Phys. 75, 69–99 (2000)

Meteorology and Atmospheric Physics

[1] Air Traffic Services Division, Civil Aeronautics Administration, Taipei, Taiwan
[2] North Carolina State University, Raleigh, NC

Effects of shear and sharp gradients in static stability on two-dimensional flow over an isolated mountain ridge

Ting-An Wang[1] and **Yuh-Lang Lin**[2]

With 14 Figures

Received September 25, 1999
Revised February 9, 2000

Summary

We have investigated the effects of shear and sharp gradients in static stability and demonstrated how a mountain wave and its associated surface winds can be strongly influenced. Linear theory for two-dimensional, nonrotating stratified flow over an isolated mountain ridge with positive shear and constant static stability shows that the horizontal wind speeds on both the lee and upslope surfaces are suppressed by positive shear. The critical $F(= U/Nh$ where U is the basic wind speed, N the Brunt-Vaisala frequency, and h the mountain height) for the occurrence of wave breaking decreases when the strength of the positive shear increases, while the location for the wave-induced critical level is higher in cases with larger positive shear. The linear theory is then verified by a series of systematic nonlinear numerical experiments. Four different flow regimes are found for positive shear flow over a two-dimensional mountain. The values of critical F which separate the flow regimes are lower when the strength of the positive shear is larger. The location of stagnation aloft from numerical simulations is found to be quite consistent with those predicted by linear theory.

We calculate the strongest horizontal wind speed on the lee surface ($U_{\max}$), the smallest horizontal wind speed on the upslope surface ($U_{\min}$), the reflection (Ref), and the transmission (Tran) coefficients for different combinations of the stability ratio between the upper and lower layers (i.e. $\lambda_{12} = N_2/N_1$) and z_1 (interface height) in a two-layer atmosphere from linear analytical solutions. Both Ref and Tran are found to be functions of $\log(\lambda_{12})$ but not the interface height (z_1). Ref is larger when λ_{12} is much different from 1, no matter whether it is larger or smaller than 1. However, Tran decreases when $\log(\lambda_{12})$ increases and approaches 0 when $\log(\lambda_{12})$ is large. The magnitude of the largest $U_{\max}$ (smallest $U_{\min}$) increases (decreases) as the absolute value of $\log(\lambda_{12})$ increases. It is found that the largest $U_{\max}$ occurs when the nondimensional z_1 is near $0.25 \pm n/2$ for cases with a less stable upper layer or when z_1 is near $n/2$ for cases with a more stable upper layer. These results are confirmed by nonlinear numerical simulations. We find that linear theory is very useful in qualitative analysis of the possibility of high-drag state for different stability profiles. The location of stagnation aloft in a two-layer atmosphere from numerical simulations agrees very well with those predicted by linear theory.

The above findings are applied to investigate the Boulder severe downslope windstorm of 11 January 1972. We find that the windstorm cannot develop if the near mountain-top inversion is located at a higher altitude (e.g., $z = 6.7$ km). However, if there exists a less stable layer right below the tropopause, the windstorm can develop in the absence of a low-level inversion. These results indicate the importance of partial reflection due to the structured atmosphere in influencing the possibility of severe downslope windstorms, although partial reflection may not be the responsible mechanism for the generation of windstorms.

1. Introduction

Recently, Lin and Wang (1996, denoted as LW hereafter), using a numerical model, identified four flow regimes for two-dimensional, hydrostatic, nonrotating, continuously stratified, uniform Boussinesq flow over an isolated mountain ridge: (I) flow with neither wave breaking aloft nor upstream blocking ($F \geq 1.12$), (II) flow with

wave breaking aloft in the absence of upstream blocking ($0.9 < F \leq 1.12$), (III) flow with both wave breaking and upstream blocking, but where wave breaking occurs first ($0.6 < F \leq 0.9$), and (IV) flow with both wave breaking and upstream blocking, but where blocking occurs first ($0.3 \leq F \leq 0.6$). The control parameter F is defined as U/Nh, where U is the undisturbed horizontal wind speed of the far upstream basic flow, N is the Brunt-Väisälä frequency, and h is the peak mountain height of a bell-shaped obstacle. The critical $F(F_c)$ which separates regimes I and II in their numerical study is very close to 1.18 ($F_c^{-1} = 0.85$), which was also found by Miles and Huppert (1969) based on Long's nonlinear analytical solution (Long, 1953). The small discrepancy between F_c obtained numerically and theoretically is explained by Wang (1996) to be due to the modification of upstream flow conditions during the integration of the numerical model over a finite domain. If the horizontal domain of the numerical model is increased, the numerical value of F_c is found to be even closer to the analytical value 1.18. Basically, LW verifies the finding of Miles and Huppert (1969) in determining F_c which separates linear mountain waves from the high-drag state (Peltier and Clark, 1979) flow behavior. Prior to the study of LW, F_c was proposed to be different from the theoretical value 1.18 in some other studies, e.g. $F_c = 1.33$ for flow past a Gaussian mountain in numerical simulations by Pierrehumbert and Wyman (1985) and $F_c = 0.67$ in laboratory experiments by Baines and Hoinka (1985).

The purpose of the present study is to extend LW's study to include the effects of vertical shear and sharp gradients in static stability, which are commonly observed in the real atmosphere. According to the observational data (e.g., Fig. 12 of Peltier and Clark, 1979), the horizontal wind speed increases almost linearly with height in the troposphere during winter, the season in which severe downslope windstorms are most frequent at Boulder, Colorado. Sharp, vertical gradients in static stability also often exist in the atmosphere, and this structure modifies the nature of a mountain-induced disturbance significantly. The tropopause and boundary layer capping inversions are examples of stability structures found in the atmosphere.

The nondimensional critical mountain height ($F_c^{-1} = Nh/U$) for stagnation aloft and along the upslope lower boundary were investigated by Smith (1989) theoretically for stratified forward shear flow past a three-dimensional isolated mountain in isosteric coordinates. It was shown that F_c^{-1}, if the surface wind speed is taken as U in calculating F_c^{-1}, for both stagnation aloft and along the upslope surface is a function of the aspect ratio (h/a, where a is the horizontal scale of the mountain) and Richardson number (Ri). The mountain height needed for stagnation at the lower boundary is modified very little by the presence of shear. However, the increasing ambient wind speed with height reduces the possibility of stagnation and wave breaking aloft. If reversed wind shear exists and continues aloft, the ambient flow must decrease to zero at some level. Such flows have been analyzed using linear theory (Booker and Bretherton, 1967), revealing that near the wind reversal level (i.e., the critical level in a steady-state flow) gravity waves are absorbed in such a way that requires viscous or nonlinear effects, even for a nearly inviscid fluid and an infinitesimal hill. The effects of reversed wind shear with a critical level on two-dimensional orographically-forced flow responses are investigated in a separate in a separate study (Wand and Lin, 1999a, b). In this study, the role of forward shear in influencing the flow response is investigated rigorously using a nonlinear numerical model and explained using a two-dimensional linear theory. One of the objectives is to study how the flow regime is modified when there exists wind shear in the atmosphere in order to improve the prediction of severe downslope windstorms.

If the stability varies with height, one can approximate the $N(z)$ structure as a number of discrete layers of constant N in certain cases. At the sharp interfaces between such layers, partial reflections must occur to allow the pressure and vertical velocity fields to remain continuous (Blumen, 1965; Klemp and Lilly, 1975). Klemp and Lilly (1975) suggested that a strong surface response occurs whenever the depth of the troposphere is an integral number of half the mean vertical wavelength of the disturbance. Under such conditions there is constructive interference between the direct wave from the surface and the partially reflected wave from the

tropopause, and a modest increase in the surface response. From their point of view, then, the occurrence of a windstorm demands a rather special tuning of the mean flow parameters. Chun (1995) studied the response of a stably stratified two-layer atmosphere to low-level heating. She found that the incident wave from lower levels may be totally reflected from the interface if the upper layer is neutrally stratified. The flow response is controlled by the low-layer depth and the stability ratio between the upper and lower layers. Chun's study used a uniform upstream wind profile. In this study, we will investigate the wave reflection and transmission in a structured shear flow.

Scorer (1949) was the first to adopt a two-layer atmosphere in the study of a stratified flow over mountains. The interface condition is based on the continuity of the solution and its first derivative. Scorer's conditions are of considerable importance because they suggest the kind of airstream structure which favors lee (resonance) waves. The criterion for the occurrence of lee waves and the factors which govern the amplitude of the waves are proposed in his study. Lee waves do not decay downstream, but the amplitude of the disturbance does fall off rapidly with height (Smith, 1979). In practice, Scorer's condition for the existence of lee waves is associated with a strongly stable layer in the lower atmosphere and/or strongly increasing wind speed with height. In the stable lower layer, the generated wave propagates up and to the right. Eventually it reaches the reflection level with $k^2 > l^2$, where k is the horizontal wave number and l^2 is the Scorer parameter. The wave cannot propagate above this level, and the wave energy is totally reflected back toward the ground. Thus, the wave energy oscillates between the ground and the reflection level, forming a standing wave pattern in the vertical (i.e., no phaseline tilt). The use of Scorer's criterion has been proved successful, at least in a statistical sense, for predicting the occurrence of lee waves.

Queney et al. (1960) showed that most of the very short waves ($k \to \infty$) and about 75% of the very long waves ($k \to 0$) are able to pass through the tropopause without reflection, while approximately 25% of the very long waves are reflected back to the ground from the tropopause. They also found that the amplitude of the long-wave components in the stratosphere is profoundly influenced by the flow parameters in the troposphere. Corby and Sawyer (1958) showed that Scorer-type waves were virtually independent of the flow parameters in the stratosphere.

The phase of the reflected waves is important to the flow field. A reviewed in Smith (1989), a vertically propagating wave encountering a sudden increase or decrease in static stability is partially reflected with a phase shift π or 0, respectively. The downward reflected wave returns to the lower boundary and is there reflected upward. If this reflected wave is generally in phase with the original wave generated by the topography so that the total phase shift in near 2π or an integral multiple, then the atmosphere is said to be ''tuned''. On the other hand, if the total phase shift is $\pi + 2n\pi$, the waves are out of phase and the atmosphere is ''detuned''. In principle, a tuned (detuned) atmosphere can give rise to much stronger (weaker) mountain waves than an atmosphere with no structure for a given mountain. The concept of a tuned atmosphere is primarily limited to two-dimensional hydrostatic flow. The linear theory of tuned atmospheres is now quite widely known, but it has not been proven to be useful in many applications, even for nearly two-dimensional hydrostatic flow. Smith (1989) suggested the reason for this is that the structured atmosphere is very sensitive to nonlinear effects, much more so than an unstructured atmosphere. The numerical calculations by Durran (1986) indicate that nonlinear effects begin surprisingly early in atmospheres with sharp gradients in static stability. However, we will show in this paper that linear theory is actually very useful, in a sense, for qualitative analysis of the flow response even when the flow is highly nonlinear. The sensitivity of layered flows to nonlinear effects is explained by noting the sensitivity of flow tuning to the interface height in a systematic comparison between the results predicted by both linear theory and nonlinear numerical simulations.

The remainder of the paper is organized as follows. The description of the numerical model adopted in this study is presented in Sect. 2. In Sect. 3, the effects of shear on flow regimes are demonstrated in the numerical simulations and explained by linear theory. Section 4 contains the discussion of the effects of sharp vertical gradients in static stability. The findings in both

Sects. 3 and 4 are then applied to investigate the Boulder severe windstorm of 11 January 1972 in Sect. 5. Concluding remarks are presented in Sect. 16.

2. Numerical model and experiment design

The numerical model adopted in this study is identical to that developed in LW. For convenience, the model will be briefly described in this paper. This two-dimensional, hydrostatic version of the North Carolina State University geophysical fluid dynamics model is based on the nonlinear primitive equations governing orographically forced finite-amplitude perturbations in a uniform, nonrotating, stratified, Boussinesq flow in the terrain-following coordinate $\sigma = z_T(z - z_s)/(z_T - z_s)$, where $z_s(x)$ is the mountain geometry and z_T is the top of the computational domain. The horizontal momentum, hydrostatic, incompressible continuity, and thermodynamic energy equations are

$$\frac{\partial u'}{\partial t} + u\left(\frac{\partial u'}{\partial x} + G\frac{\partial u'}{\partial \sigma}\right) + Hw'\frac{\partial u}{\partial \sigma} + \frac{1}{\rho_0}\left[\frac{\partial p'}{\partial x} + G\frac{\partial p'}{\partial \sigma}\right] + \nu u' = D_u, \quad (1)$$

$$\frac{1}{\rho_0}\frac{\partial p'}{\partial \sigma} = \frac{g\theta'}{H\bar{\theta}}, \quad (2)$$

$$\frac{\partial u'}{\partial x} + G\frac{\partial u'}{\partial \sigma} + H\frac{\partial w'}{\partial \sigma} = 0, \quad (3)$$

$$\frac{\partial \theta'}{\partial t} + u\left(\frac{\partial \theta'}{\partial x} + G\frac{\partial \theta'}{\partial x}\right) + Hw'\frac{\partial \theta}{\partial \sigma} + \nu\theta' = 0, \quad (4)$$

where

$$G = \left(\frac{\partial \sigma}{\partial x}\right)_z = \frac{\sigma - z_T}{z_T - z_s}\frac{\partial z_s}{\partial x}; \quad H = \frac{\partial \sigma}{\partial z} = \frac{z_T}{z_T - z_s}.$$

A first-order closure formulation of the subgrid mixing which depends on the relative strengths of stratification and shear (Lilly, 1962; Durran and Klemp, 1982) is adopted in this model. The subgrid scale effects are introduced into the calculations through the terms D_u and D_θ,

$$D_u = (K_M A)_x + G(K_M A)_\sigma + H(K_M B)_\sigma;$$

$$D_\theta = [K_H(\theta_x + G\theta_\sigma)]_x + G[K_H(\theta_x + G\theta_\sigma)]_\sigma + (K_H H\theta_\sigma)_\sigma,$$

where

$$A = u_x + Gu_\sigma - Hw_\sigma; \quad B = Hu_\sigma + w_x + Gw_\sigma,$$

$$K_M = k^2\Delta x\Delta z|\mathrm{Def}|\left[\max\left(1 - \frac{K_H}{K_M}R_i, 0\right)\right]^{1/2},$$

$$R_i = N_L^2/\mathrm{Def}^2, \quad \mathrm{Def}^2 = A^2 + B^2,$$

$$N_L^2 = g\frac{\partial}{\partial \sigma}[\ln(\theta)].$$

In this study, we assume that $k = 0.21$ and $K_H/K_M = 3$ as suggested by Deardorff (1971, 1972). Some symbols are explained below, while others have their conventional meanings:

u	total horizontal velocity
U	basic horizontal velocity
u'	perturbation horizontal velocity
w'	vertical velocity
p'	perturbation pressure
θ	total potential temperature
$\bar{\theta}$	basic state potential temperature
θ'	perturbation potential temperature
ν	coefficient of Rayleigh friction and Newtonian cooling
ρ_0	constant reference density
T_0	constant reference temperature
K_H	eddy diffusivity of heat
K_M	eddy diffusivity of momentum
R_i	Richardson number
N_L	local Brunt-Väisälä frequency.

In deriving Eq. (1), the hydrostatic equation has been used. The governing equations are discretized and numerically integrated over a two-dimensional grid in (x, σ) space. The horizontal (vertical) derivatives are approximated by fourth (second)-order centered differences. These schemes are identical to those employed in the Cartesian model adopted by Lin et al. (1993), and Wang et al. (1996). The time derivatives are approximated through the leapfrog scheme, with the exception of the first time step, which is computed by forward differencing. Viscous effects are modeled through the inclusion of Rayleigh friction and Newtonian cooling, which for all cases reported in this paper are taken to be zero in the model physical domain.

Within the terrian-following coordinate system, the lower boundary condition requires $w' = udh/dx$ at $\sigma = 0$, where h is the terrain function. The upper boundary condition is approximated

either by placing an artificial viscous absorbing layer (Klemp and Lilly, 1978) or imposing the radiation boundary condition (Klemp and Durran, 1983) at the top of the physical domain. In the present model, the damping in the sponge layer is associated with Rayleigh friction and Newtonian cooling. To minimize wave reflection, the damping coefficient ν is increased gradually from zero at the top of the inviscid region, $z = z_1$, to z_T at the top boundary, $z = z_T$, according to

$$\nu = \nu_T \sin^2\left(\frac{\pi}{2}\frac{z - z_1}{z_T - z_1}\right). \tag{5}$$

The numerical technique for implementing the radiation upper boundary condition can be found in Klemp and Durran (1983). In this study, we use the viscous absorbing layer since it is more reliable in simulating flow over mountains (Wang, 1996). The lateral boundary conditions are specified by the Orlanski (1976) radiation condition. A five-point numerical smoother (Shapiro, 1970) is applied to every field at every time step to damp $2\Delta x$ waves, while a three-point numerical smoother is applied to damp $2\Delta t$ waves (Asselin, 1972).

The time and horizontal grid intervals used in this study are 10 s and 4 km, respectively. For all cases presented in this study, the horizontal domain contains 128 grid points. There are 80 vertical grid intervals. An idealized bell-shaped mountain ridge is used throughout this study,

$$h_s(x) = \frac{h}{(x/a)^2 + 1}, \tag{8}$$

where h and a are the mountain height and half-width, respectively. The mountain half-width is taken as 20 km in this study except in Sect. 5 where it is reduced to 10 km. This model has been tested against Long's nonlinear theoretical results and the nonhydrostatic model results of Peltier and Clark (1979), and is found to be capable of producing accurate results (see LW).

3. Shear effects on flow regimes for two-dimensional orographically-forced flow

a) Linear flow

In this section, we investigate the effects of wind shear on the two-dimensional response for stratified flow over a mountain ridge. We first discuss the linear analytical results. If the basic wind profile is specified as $U(z) = U_0 + \alpha z$, where U_0 is the wind speed at $z = 0$, and $N(z) = N$, where N is the Brunt-Väisälä frequency, the solutions can be calculated following the procedures similar to those in Smith (1986). For details, readers are referred to that paper. The steady-state perturbation horizontal and vertical wind velocities can be obtained by

$$u'(x,z) = \frac{-U_0 haH^{-1/2}(z+H)^{-1/2}}{a^2 + x^2} \times \left[\left(\frac{a}{2} - \mu x\right)\cos\theta + \left(\frac{x}{2} + \mu a\right)\sin\theta\right], \tag{9}$$

$$w'(x,z) = \frac{U_0 haH^{-1/2}(z+H)^{1/2}}{(a^2 + x^2)^2} \times [(a^2 - x^2)\sin\theta - 2ax\cos\theta], \tag{10}$$

where $H = U_0/\alpha$, $\mu = \sqrt{R_i - 0.25}$, $\theta = \mu \ln(\frac{H}{H+z})$, and $Ri = (N/a)^2$. These steady-state solutions for two-dimensional nonrotating flow are plotted in Fig. 1 for $F = U_0/Nh = 10$, and $Ri = \infty$ (Figs. 1a–b), 100 (Figs. 1c–d), and 10 (Figs. 1e–f). In this figure, the vertical domain is $3.4\lambda_z$, where $\lambda_z = 2\pi U_0/N$. For the uniform flow case, vertically propagating waves are predicted by the theory, whose amplitudes vertically repeat every λ_z. Note that this local vertical wavelength only holds under conditions suitable for the WKB approximation. It is well known that the extreme magnitude of disturbance occurs somewhere along the vertical line above the mountain peak ($x = 0$) for linear hydrostatic mountain waves. For cases with forward shear in the wind profile, vertically propagating mountain waves are also observed, similar to those produced in uniform flow. However, the local vertical wavelength increases with height since it is calculated by $2\pi U(z)/N$. In the case with $Ri = 100$, the whole domain contains about 1.6 vertical wave cycle, while it contains only about 1 vertical wave cycle in the case with $Ri = 10$. The extreme magnitude of disturbance in $u'(w')$ decreases (increases) with height instead of vertically repeating with the same value unlike the case with uniform basic wind. This may be explained, to a first approximation, by the linearized momentum and thermodynamic equations in Fourier space where w' is proportional to and u' is inversely propor-

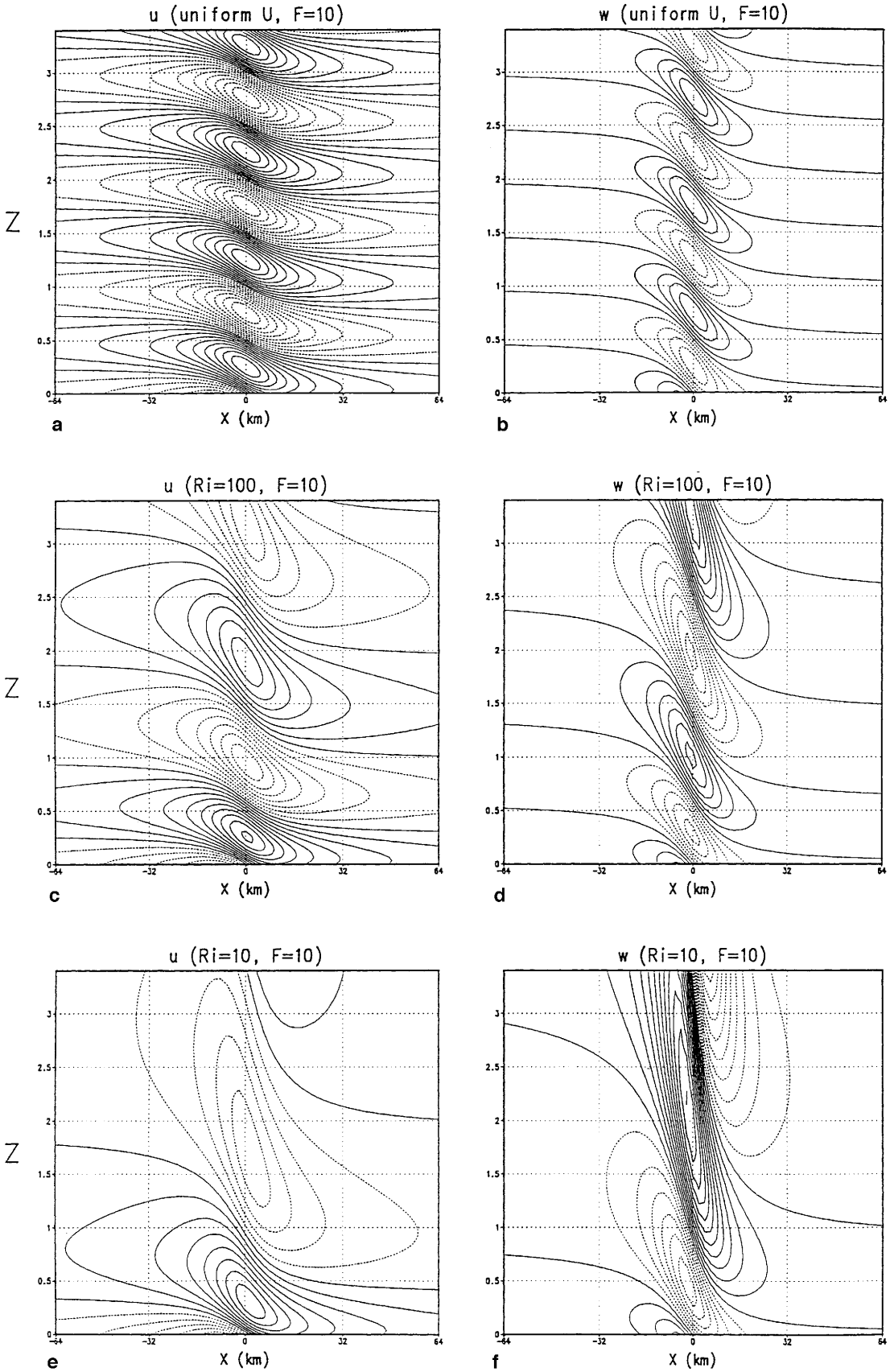

Fig. 1. **a** The horizontal perturbation wind field from the analytical solution for uniform flow over a bell-shaped mountain; **b** same as in **a** except for vertical wind field; **c** same as in **a** except for shear flow with $Ri = 100$ from Eq. (9); **d** same as in **c** except for vertical wind field; **e** same as in **c** except with $Ri = 10$; **f** same as in **d** except with $Ri = 10$

tional to the basic wind speed, which increases with height. One of the objectives of this study is to discuss the effects of shear on the occurrence of severe downslope winds. It is well-known that the first stage of severe downslope winds is the existence of stagnation aloft or a wave-induced critical level (e.g., Scinocca and Peltier, 1993). In cases with uniform flow (Fig. 1a), the lowest stagnation aloft is located near $z = 0.75\lambda_z$ where u' is minimum (e.g., see Peltier and Clark, 1979). Wind reversal will occur when $u' + U_0 < 0$. However, the height of the lowest stagnation aloft in Figs. 1c and e must be located at a higher altitude than that in Fig. 1a, since the local vertical wavelength increases as the shear increases (*Ri* is smaller).

Since the extreme magnitude of u' for cases with forward shear occurs somewhere along the vertical line at $x = 0$, the location of minimal u' along this line can be calculated from Eq. (9) with $x = 0$,

$$u'(0,z) = -U_0 h H^{-1/2}(z+H)^{-1/2} \times \left[\mu \sin\theta + \frac{\cos\theta}{2}\right], \tag{11}$$

and by taking the derivative of $u'(0,z)$ with respect to z. The value of z for which $\partial u'(0,z)/\partial z = 0$ is the location where $u'(0,z)$ has either a local maximum or minimum. We define z_c as the value which causes $u'(0,z)$ to be a minimum. Adopting this strategy, z_c can be obtained

$$z_c = \frac{\sqrt{R_i}}{2\pi}[e^{3\pi/2\mu} - 1]. \tag{12}$$

Notice that z_c in Eq. (12) has been normalized by $2\pi U_0/N$ and approaches the value 0.75 as *Ri* approaches infinity (shown in Fig. 2c). The case with infinite *Ri* can be considered as the one with uniform flow, the value of 0.75 is consistent with that predicted by linear theory for orographically-forced uniform flow (e.g., Peltier and Clark, 1979). Substituting the value of z_c into Eq. (11), we can obtain the minimal value $u'(0,z_c)$. When overturning occurs, total horizontal wind speed $u'(0,z_c) + U_0 + \alpha z_c \leq 0$. Therefore, F_c for the existence of stagnation aloft can be obtained.

$$F_c = \frac{\mu}{\sqrt{R_i}} e^{-9\pi/4\mu}. \tag{13}$$

Other dynamically important variables are the strongest horizontal wind speed at the lee surface and the smallest horizontal wind speed at the upslope surface. The latter is related to the possibility of stagnation occurring at the lower boundary. The perturbation horizontal wind speed at the surface can be obtained from Eq. (9)

$$u'(x,0) = \frac{-U_0 h a H^{-1}}{a^2 + x^2}\left[\frac{a}{2} - \mu x\right]. \tag{14}$$

From Eq. (14), the maximum ($U_{\max}$) and minimum ($U_{\min}$) horizontal wind velocities at the surface normalized by U_0 can be obtained

$$U_{\max} = 1 + \frac{1}{F}\left[\frac{1}{2} - \frac{1}{4\sqrt{Ri}}\right], \quad z = 0 \tag{15}$$

and

$$U_{\min} = 1 - \frac{1}{F}\left[\frac{1}{2} + \frac{1}{4\sqrt{Ri}}\right], \quad z = 0, \tag{16}$$

respectively. The results from Eqs. (12)–(16) are plotted in Fig. 2. Figure 2a shows the variation of $U_{\max}$ at the lee surface with *Ri* for cases with $F = 1$. It is apparent that $U_{\max}$ decreases as the shear increases (*Ri* decreases). Figure 2b shows the variation of $U_{\min}$ at the upslope surface with *Ri* for cases with $F = 1$. Similar to Fig. 2a, $U_{\min}$ decreases as *Ri* decreases. For two-dimensional flow, upstream blocking occurs when there exists a stagnation at the upslope surface. From Fig. 2b (or Eq. 16), it can be determined that forward shear increases the possibility of upstream blocking. However, if we calculate the critical F for upstream blocking based on the value of $U_{\min}$, it is found that the modification is not very significant when $Ri \leq 10$. The decrease in $U_{\min}$ may be due to positive vorticity induced in the y-direction by the forward shear. The vorticity of the basic wind alters the low-level circulation. Smith (1979) suggested that low-level blocking is one of the most important ways in which mountains affect the airflow. The most powerful method for understanding nonlinear mountain flows is by direct numerical integration of the governing equations. The application of linear steady-state theories is limited to a few illustrative examples because the regime diagrams are not thoroughly known.

Figure 2c shows the variation of z_c with *Ri* from Eq. (12). It is found that z_c increases as *Ri* decreases. When *Ri* is very large, then z_c is close to 0.75, which is the location of wave-induced critical level for the uniform flow case. Figure 2d

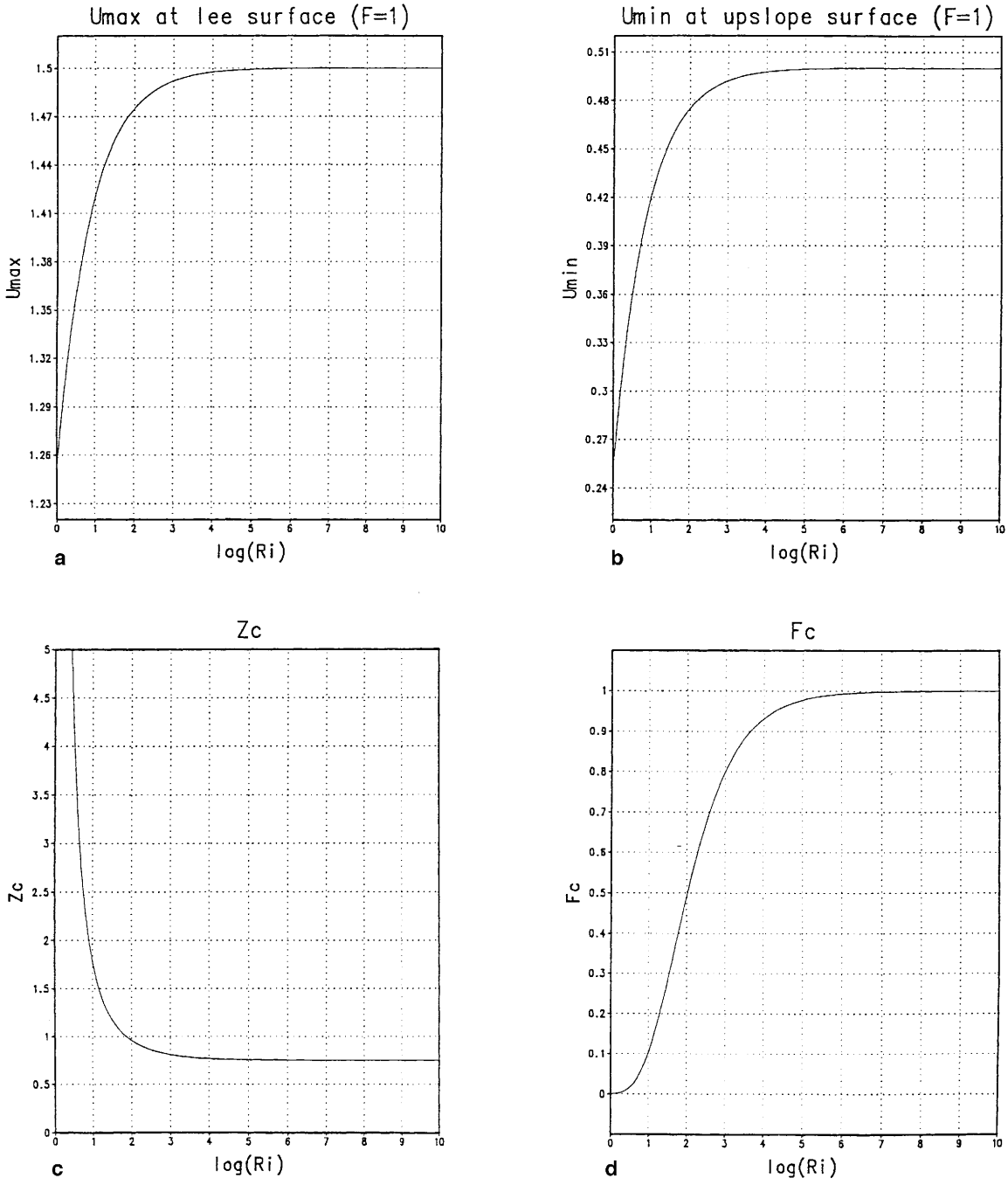

Fig. 2. a The strongest horizontal wind speed at the lee surface from Eq. (15); **b** the smallest horizontal wind speed at the upslope surface from Eq. (16), **c** the location of stagnation aloft from Eq. (13), and **d** the critical F for wave breaking as functions of Ri in shear flow

shows the variation of F_c with Ri from Eq. (13). It is apparent that F_c decreases as Ri decreases. This is consistent with that proposed by Smith (1989) for three-dimensional flow over an isolated mountain; that increasing ambient wind speed aloft reduces the possibility of wave breaking. When Ri is very large, F_c approaches 1 which is the critical F for the uniform flow case predicted by linear theory. As aforementioned in the Introduction, F_c is predicted by nonlinear theory to be 1.18 (Miles and Huppert, 1969) as verified by nonlinear numerical simulations (e.g., LW) for uniform flow over a two-dimensional bell-shaped mountain ridge. The discrepancy of F_c in linear

theory is due to the linear assumption and the use of a linear lower-boundary condition (Laprise and Peltier, 1989). Although the F_c from linear theory is not quite accurate, we will show later from the results of nonlinear numerical simulations that the curve shown in Fig. 2d is able capture the tendency of the influence of shear on the flow regime.

b) Nonlinear flow

We now adopt the numerical model described in Sect. 2 to conduct experiments for studying the effects of shear on two-dimensional, nonrotating, orographically-forced flow. In the experiments considering the effects of shear, the parameters are specified as follows: $U_0 = 10\,\mathrm{ms}^{-1}$, $N = 0.01\,\mathrm{s}^{-1}$, and varying peak mountain height (h) and wind shear strength (α). In these experiments, two nondimensional control parameters, $F = U_0/Nh$ and $Ri = (N/\alpha)^2$, govern the hydrostatic flow response for a constant aspect ratio (h/a). F varies from 0.5 to 1.2, and Ri is chosen to be either 20, 100, 400, 900, infinity, 900^- (superscript denotes those cases with backward shear) or 400^-. The corresponding h and α for a certain case can be calculated from F, U_0, N, and α. Note that $\alpha < 0$ when backward shear is considered. The experiments with backward shear are conducted in order to further verify some conclusions we draw from cases with forward shear. However, we will not discuss the cases of backward shear with a critical level in this study. Since the vertical domain of the numerical model is finite, we can calculate the wind speed at top of the domain in advance to avoid the case with a critical level when backward shear is considered. The major interest in this section is the role of forward shear. The effects of critical level on severe downslope winds will be studied in a separate paper (Wang and Lin, 1999b). In all the experiments in this section, the mountain half-width is taken as 20 km.

Table 1 shows the nondimensional time for the occurrence of wave breaking (T-break) and upstream blocking (T-block). T-break and T-block are defined as the time at which the total horizontal velocity becomes zero aloft and along the upslope surface, respectively. F is the only flow regime control parameter if uniform U and N are considered for hydrostatic airflow over a mountain as shown in LW. Notice that as α approaches 0, our solution approaches those in LW. As proposed by LW, the results for cases with uniform flow can be separated into four flow regimes: (I) flow with neither wave breaking aloft nor upstream blocking (e.g., $F = 1.2$), (II) flow with wave breaking aloft in the absence of upstream blocking (e.g., $F = 1.1, 1.0$), (III) flow with both wave breaking and upstream blocking, but where wave breaking occurs first (e.g., $F = 0.9, 0.8, 0.7, 0.6$), and (IV) flow with both

Table 1. The nondimensional time for the occurrence of wave overturning aloft (bold numbers) and upstream blocking (italicized numbers) for different F and Ri

F \ Ri	20	100	400	900	infinity ($\alpha = 0$)	900^- ($\alpha < 0$)	400^- ($\alpha < 0$)
1.2	**No**	**No**	**No**	**No**	**No**	**11.25**	**9.77**
	No	*No*	*No*	*No*	*No*	*No*	*No*
1.1	**No**	**No**	**No**	**33.54**	**13.07**	**9.31**	**8.33**
	No	*No*	*No*	*No*	*No*	*No*	*No*
1.0	**No**	**No**	**No**	**17.59**	**10.20**	**7.97**	**7.21**
	No	*No*	*No*	*No*	*No*	*No*	*No*
0.9	**No**	**No**	**14.01**	**11.77**	**8.46**	**6.86**	**6.19**
	No	*No*	*No*	*46.12*	*49.58*	*25.91*	*25.90*
0.8	**No**	**No**	**10.34**	**9.24**	**7.12**	**5.81**	**5.37**
	No	*No*	*No*	*26.08*	*19.50*	*13.50*	*12.49*
0.7	**No**	**No**	**7.91**	**7.35**	**5.89**	**4.92**	**4.58**
	No	*No*	*21.52*	*13.98*	*10.92*	*7.98*	*7.46*
0.6	**No**	**11.16**	**6.41**	**5.85**	**4.79**	**4.12**	**3.94**
	No	*No*	*5.04*	*7.53*	*5.07*	*4.72*	*4.51*
0.5	**No**	**6.51**	**5.06**	**4.66**	**3.91**	**3.40**	**3.27**
	No	*2.78*	*3.55*	*3.20*	*3.15*	*2.95*	*2.90*

wave breaking and upstream blocking, but where blocking occurs first (e.g., $F = 0.5$). For convenience in discussion, we define F_1, F_2, F_3 as the critical F values which separate flow regimes I and II, II and III, and III and IV, respectively. From Table 1, F_1, F_2 and F_3 for cases with $\alpha = 0$ are the same as proposed by LW. However, if forward shear is taken into consideration, it takes a longer time for wave breaking to occur when Ri decreases (α increases) for a certain F. For example, when $F = 0.9$, T-break = 8.46 for the case with $\alpha = 0$, while T-break = 11.77, 14.01 in cases with $Ri = 900$, and 400, respectively. Thus, F_1 decreases as the shear increases. This is consistent with that predicted by linear theory (Fig. 2d); that increasing ambient wind speed aloft reduces the possibility of wave breaking. What about F_2 and F_3, which are involved with the occurrence of upstream blocking? Basically, the time for the occurrence of upstream blocking is delayed as forward shear increases. However, careful readers may notice that cannot be applied to cases with: (1) $F = 0.6$, $Ri = 900$ to 400 and (2) $F = 0.5$, $Ri = 400$ to 100. In these cases, T-block decreases as α increases for a fixed F. Notice that both cases are located in regime IV where upstream blocking occurs prior to wave breaking. According to linear theory, forward shear magnitude increases the possibility of upstream blocking since $U_{\min}$ is smaller when Ri is smaller (Fig. 2b). Values of $U_{\min}$ found from numerical simulations (not shown) for cases with $F = 1.2$ at different Ri does support those found in Fig. 2b. However, the implication of Fig. 2b for the possibility of upstream blocking apparently does not apply to cases with smaller F (as shown in Table 1) since upstream blocking was not observed in the cases with $Ri = 20$ even when $F = 0.5$. The failure of linear theory to predict the critical F for upstream blocking in the nonlinear regime may have some physical basis. As aforementioned, the decrease of $U_{\min}$ predicted by linear theory (Fig. 2b) may be due to positive vorticity generated in the y-direction by forward shear, which alters the low-level circulation. However, the effects of basic vorticity may be significantly affected or over-predicted by the perturbation vorticity generated due to strong nonlinearity.

The above discussion provides evidence for the effects of forward shear on decreasing the possibility of stagnation aloft. We may hypothesize that backward shear may have the opposite effects. Therefore, we conduct numerical experiments with backward shear, as shown in the last two columns of Table 1. When backward shear is considered, T-break and T-block are reduced compared to those for uniform flow. In other words, decreasing ambient winds enhance the possibility of stagnation both aloft and at upslope surface. F_c separating regimes I and II is about 1.35 in cases with $Ri = 900^-$ and about 1.45 in cases with $Ri = 400^-$ according to our numerical results with larger F (not shown). These two critical F are both larger than 1.18, which if F_c for the uniform flow case.

The other feature apparent in Table 1 that both T-break and T-block decrease as F decreases when a certain Ri is considered, no matter whether vertical shear exists or not. This is due to the increase in nonlinearity when F decreases, which speeds up the formation of both wave breaking and upstream blocking. Based on the above discussion, we may conclude that the major effects of shear are to modify F_1, F_2 and F_3 which separate the flow regimes. The dynamics for sheared flow are similar to those of uniform flow.

Table 2 shows the initial overturning height (z_c), which is nondimensionalized by $\lambda_z = 2\pi U_0/N$. For uniform flow cases ($\alpha = 0$), z_c increases as F decreases. The definition of z_c is the lowest height at which critical steepening occurs in the steady state solution in Laprise and Peltier (1989), while it is the height of the first detection of negative horizontal wind velocity aloft in the time integration in this study. Laprise and Peltier (1989) suggested that $z_c = 0.75(0.76)$ if a linear (nonlinear) lower boundary condition is adopted in the hydrostatic version of Long's nonlinear solution. It is well known that z_c is independent of F according to linear theory or Long's nonlinear solution. According to Table 2, z_c increases from 0.69 to 0.76 when F decreases from 1.1 to 0.5 for uniform flow. However, this variation of z_c with F is insignificant, in a sense, since z_c is always close to 0.75 for cases with $\alpha = 0$. When shear effects are considered, it is found that forward shear enlarges z_c and backward shear reduces z_c for certain F, e.g. for $F = 0.6$, z_c increases (decreases) from 0.74 in uniform flow to 1.11 (0.68) with $Ri = 100$

Table 2. The nondimensional height (z_c) of initial overturning for different F and Ri

F \ Ri	20	100	400	900	infinity ($\alpha = 0$)	900^- ($\alpha < 0$)	400^- ($\alpha < 0$)
1.2						**0.64**	**0.60**
1.1				**0.79**	**0.69**	**0.65**	**0.61**
1.0				**0.78**	**0.70**	**0.66**	**0.62**
0.9			**0.83**	**0.73**	**0.71**	**0.67**	**0.63**
0.8			**0.85**	**0.74**	**0.70**	**0.68**	**0.64**
0.7			**0.80**	**0.76**	**0.72**	**0.70**	**0.66**
0.6		**1.11**	**0.82**	**0.82**	**0.74**	**0.72**	**0.68**
0.5		**0.96**	**0.88**	**0.84**	**0.76**	**0.75**	**0.75**

($Ri = -400^-$). This is intuitively easy to imagine, since the local vertical wave length under forward (backward) shear is larger (smaller) than that for uniform flow, and the stagnation aloft usually occurs at the second phase of the horizontal wind field.

Figure 3a shows the regime diagram in $F - \log(Ri)$ space based on the results with forward shear in Table 1. The flow behavior can still be separated into four different regimes similar to those proposed by LW. However, F_1, F_2 and F_3 are functions of Ri if shear is considered. All these three critical F's decrease as the shear increases (Ri decreases). F_c (same meaning as F_1) shown in Fig. 2d, which is calculated from linear theory, should be compared with the upper curve in Fig. 3a. It can be seen that the tendency of F_1 is captured well by the linear solution, although the values are underestimated by linear theory due to the use of the linear lower boundary condition. Fig. 3b shows z_c from both numerical simulations and linear theory. The values obtained from linear theory capture the results predicted by nonlinear numerical simulations surprisingly well. Although z_c varies with F slightly, the values are always close to those predicted by linear theory.

Figure 4 shows the total horizontal wind field for cases with $F = 1.2$ for different Ri, namely, $Ri = 100, 400, 900$, infinity, 900^-, 400^- in Figs. 4a–f, respectively. For convenience, the vertical domain height is fixed as $1.7\lambda_z$, where $\lambda_z = 2\pi U_0/N$ and U_0 is the surface wind speed. As found from linear theory, the local vertical wave length actually varies with height due to the variation of the basic wind speed. The stronger

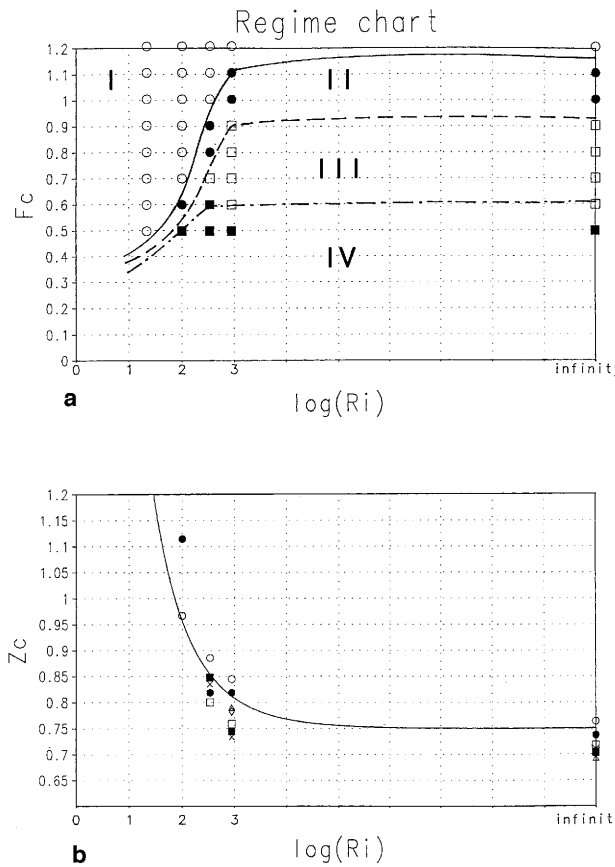

Fig. 3. a Regime diagram for 2-D, nonrotating, hydrostatic, continuously stratified forward shear flow over a bell-shaped mountain. Four flow regimes are identified: (I) flow with neither wave breaking aloft nor upstream blocking, denoted as open circles, (II) flow with wave breaking aloft and no upstream blocking, denoted as closed circles, (III) flow with both wave breaking and upstream blocking, but where breaking occurs first, denoted as open squares, and (IV) flow with wave breaking and upstream blocking, but where blocking occurs first, denoted as closed squares; **b** The comparison of nondimensional initial overturning from linear theory (solid line) and nonlinear numerical solutions

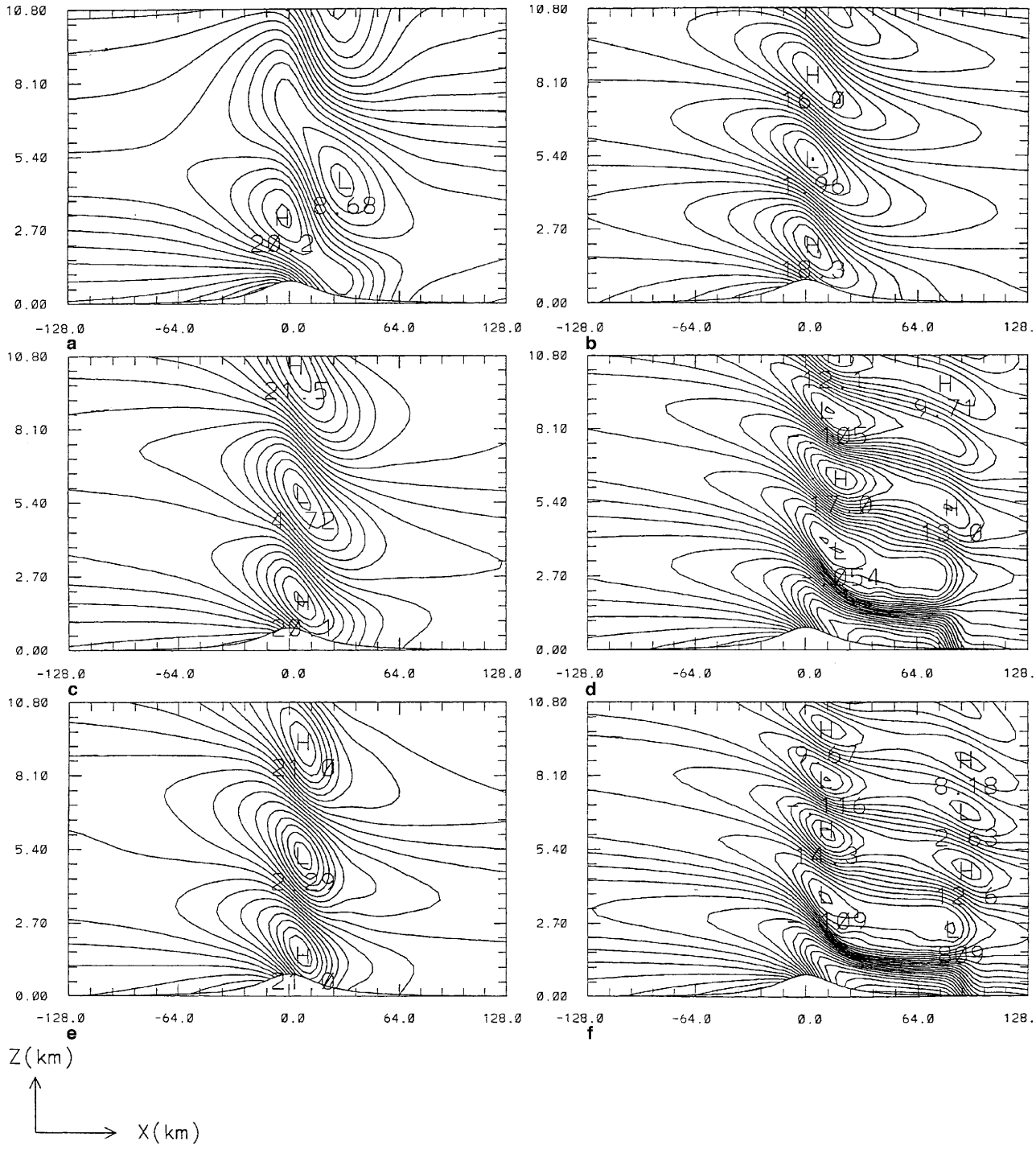

Fig. 4. The horizontal wind fields at $Ut/a = 50.4$ for the cases with $F = 1.2$, and **a** $Ri = 100$, **b** $Ri = 400$, **c** $Ri = 900$, **d** uniform basic wind, **e** $Ri = 900^-$ (with backward shear), and **f** $Ri = 400^-$

the shear of the basic wind, the larger the local vertical wavelength. The only case with constant local vertical wavelength is the one of uniform basic flow (Fig. 4d). Since wave breaking requires stagnation aloft, the minimal wind speed aloft in the case without wave breaking may be a good indicator to determine how far the flow is away from wave breaking. The minimal wind speeds (in ms^{-1}) aloft are 8.68, 4.72, 2.29, and 1.96 in Figs. 4a–d, respectively. The smaller the *Ri*, the

farther away the minimal wind speed from stagnation is. Notice that Ri increases from 100 in Fig. 4a to ∞ in Fig. 4d. Therefore, the possibility of stagnation aloft is reduced by increasing ambient wind speed. As shown in Table 1, backward shear enhances the possibility of stagnation. There exists wave breaking for cases with backward shear when $F = 1.2$ (Figs. 4e–f). The internal jump develops with the occurrence of wave overturning, and then propagates downstream to produce severe downslope winds on the lee surface. $U_{\max}$ is 2.32 in Fig. 4e and 2.36 in Fig. 4f, while it is only 1.48 in Fig. 4d. The effects of shear on the magnitude of the lee slope wind will be discussed later. No upstream blocking is observed for any case shown in Fig. 4. The behavioral characteristics of those cases in Fig. 4a–d are considered as regime I (no wave breaking and no upstream blocking), while those in Fig. 4e–f as regime II (with wave breaking, but no upstream blocking).

Figure 5 shows the horizontal wind fields for cases with $F = 1.0$ for different Ri. The only difference between this figure and Fig. 4 is the value of F. Wave breaking is observed in Fig. 5c–f, but not in Fig. 5a–b. However, there still exists no upstream blocking. Therefore, the cases shown in Fig. 5c–f are characterized as regime II, while both cases shown in Fig. 5a–b belong to regime I. If F is further decreased to 0.8, the case with $Ri = 100$ (Fig. 6a) is still characterized as regime I, but the flow with $Ri = 400$ (Fig. 6b) switches to regime II. A significant change of the flow characteristics is observed in Fig. 6c–f. There is a layer with negative horizontal wind speed above the upslope surface, which means some airflow recirculates upstream rather than passing over the mountain peak. This phenomenon is the so-called upstream blocking.

Figure 7 shows the horizontal wind field for cases with $F = 0.5$ for different Ri. Obviously, there exists both upstream blocking and wave breaking for all cases. Although the behavior of those cases with both wave breaking and upstream blocking in Figs. 6 and 7 look similar, one major difference is the time of occurrence of these two phenomena. According to Table 1, upstream blocking occurs after the existence of wave breaking for those cases shown in Fig. 6, while it occurs prior to wave breaking for those shown in Fig. 7. Therefore, the cases with both upstream blocking and wave breaking in Fig. 6 belong to regime III, while those in Fig. 7 belong to regime IV. If we look carefully, differences do exist in the flow responses in these two regimes. For example, the contour lines on the upstream side ($x < 0$) are more horizontal for those cases shown in Fig. 7 than those in Fig. 6. This may be due to the columnar disturbances (Pierrehumbert and Wyman, 1985) which propagate upstream without dispersion, modifying the basic-state profiles until $x = -\infty$.

Table 3 shows $U_{\max}$ for those simulations shown in Tables 1 and 2. Basically, $U_{\max}$ increases as F decreases for certain Ri no matter whether shear exists or not. $U_{\max}$ in regime I (denoted as regular numbers in Table 3) is much smaller compared to those in other regimes. Similar to those predicted by linear theory (Fig. 2a), $U_{\max}$ is reduced by forward shear in regime I for certain F. For example, $U_{\max}$ decreases from 1.85 to 1.36 in cases with $F = 1.2$, and from 1.93 to 1.43 in cases with $F = 1.0$ when the shear strength increases. Notice that this comparison should only be made for flows belonging to the same flow regime. $U_{\max}$ increases abruptly when F is reduced slighly (0.1) to switch flow regimes from I to II (denoted as bold numbers in Table 3). For example, $U_{\max}$ increases from 1.85 for $F = 1.2$ to 2.56 for $F = 1.1$ for the uniform flow case, and from 2.04 for $F = 0.7$ to 3.41 for $F = 0.6$ for those cases with $Ri = 100$. The increasing magnitude of $U_{\max}$ from regime I to II for the case with $Ri = 900$ is not as large as in other cases ($Ri = 100, 400$, and ∞), which is due to the delayed formation of stagnation aloft as shown in Table 1. In this case ($Ri = 900, F = 1.1$), the end of the simulation still corresponds physically to an early stage in the development of wave breaking, according to features in the horizontal wind field (not shown). In other words, $U_{\max}$ is still increasing and has not reached its maximum value yet. The increments of $U_{\max}$ responsible for transitions from regime II to III and from regime III to IV are not as significant as those from regime I to II; instead, it is more like a gradually increase due simply to the increasing nonlinearity as F decreases. This result if consistent with that found by LW. From this, it may be reasonable to conclude that the upstream blocking may not have strong effects on influencing the magnitude of downslope winds. Roughly speaking, the

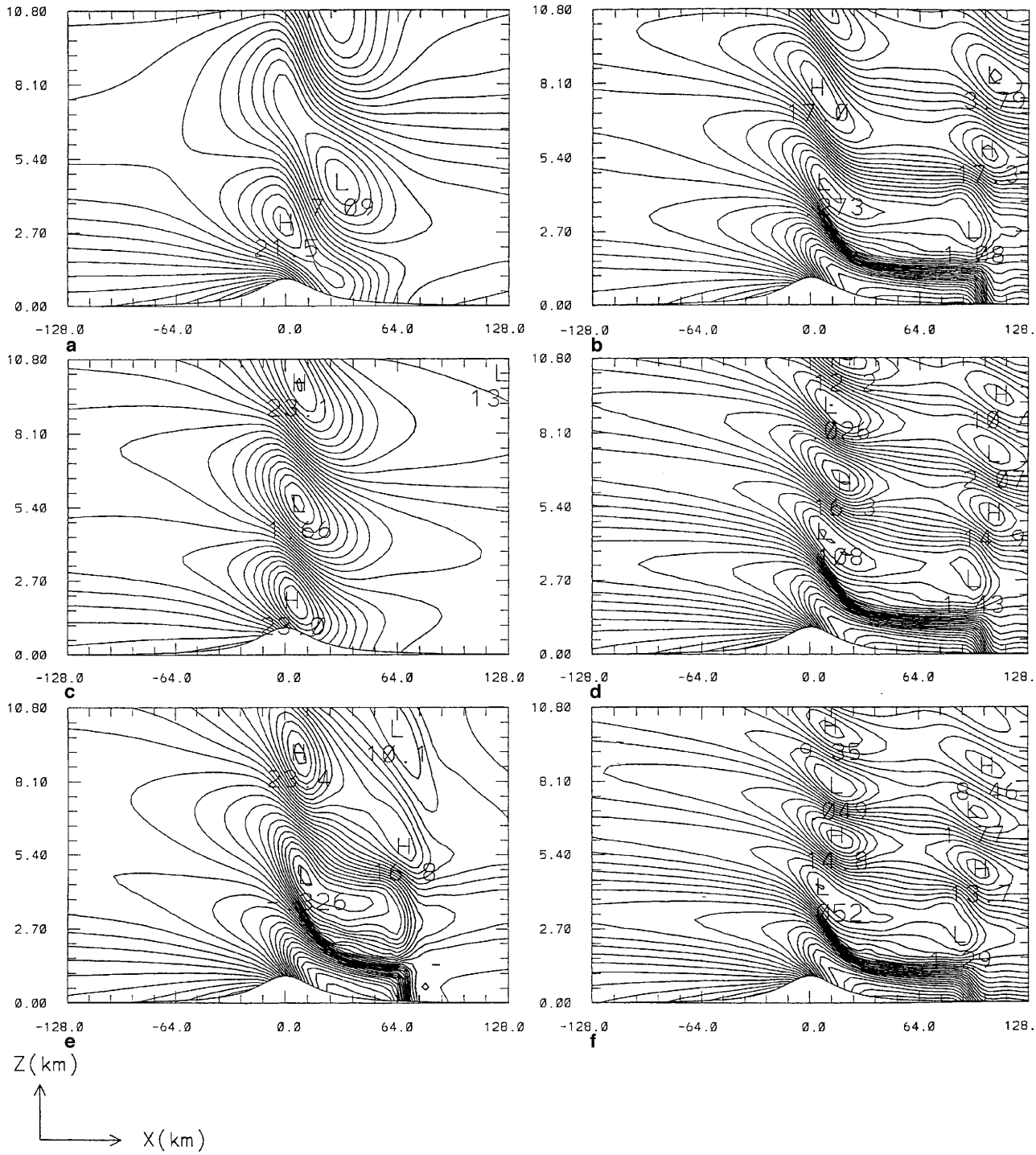

Fig. 5. Same as in Fig. 4 except with $F = 1.0$

magnitude of the downslope wind is about 2.55–3.5 times the basic wind speed at the surface when wave breaking exists. If the basic surface wind speed is 20 ms^{-1}, the downslope wind speed can be as large as 50–70 ms^{-1}, which is as strong as those which occur in a hurricane.

Surface drag (normalized by $\pi\rho U_0 N h^2/4$) is a good measure of the strength of the wave response. Miles and Huppert (1969) have shown that nonlinearity enlarges the drag values. The nonmalized surface drag based on the numerical results is shown in Table 4. For cases in regime I,

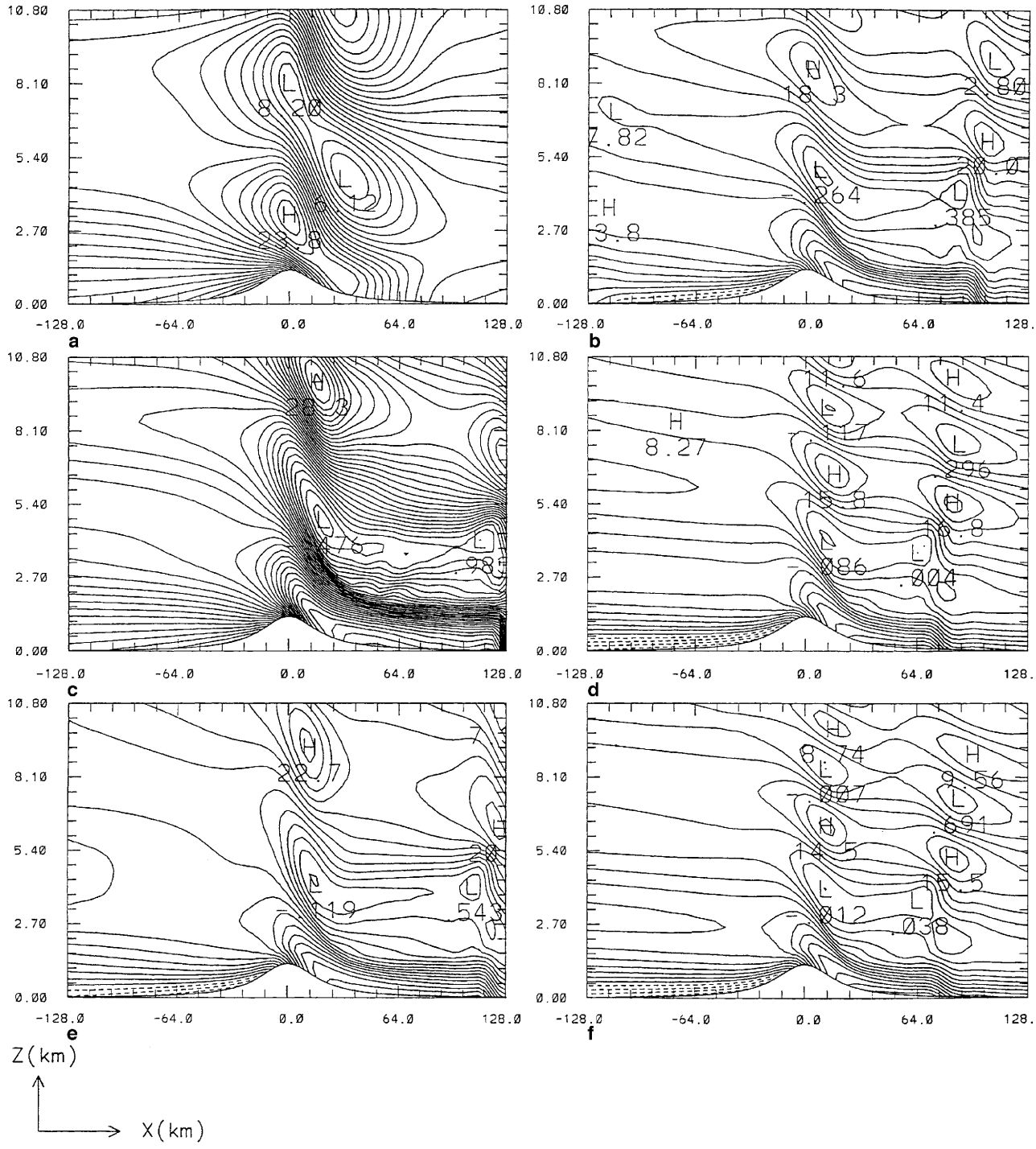

Fig. 6. Same as in Fig. 4 except with $F = 0.8$

which can be considered as either linear or weakly nonlinear, the vertical profile of the horizontal momentum flux (not shown) is almost vertical and is very close to the surface drag since there is almost no interaction between the perturbation and the basic state (Eliassen and Palm, 1996). However, a vertical gradient exists in the momentum profile between the ground and the top of the wave breaking region in other flow regimes. It has been indicated that the drag can reach several times its linear value for cases characterized as high-drag states from uniform

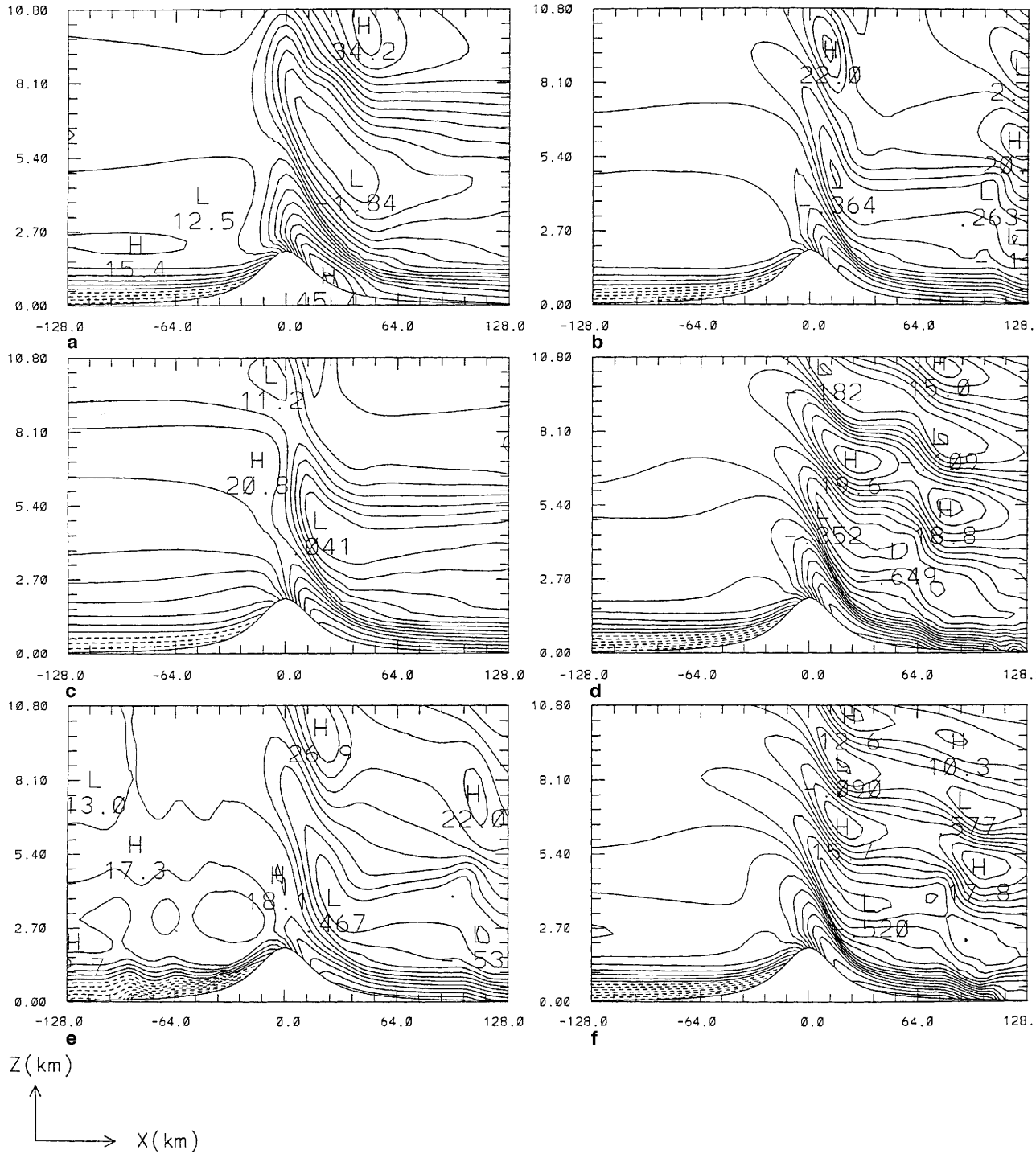

Fig. 7. Same as in Fig. 4 except with $F = 0.5$

flow experiments (e.g., Clark and Peltier, 1984). As shown in Table 4, the largest value of drag occurs in regime II with F very close to F_1. It is about four times the linear value for uniform flow and about five times for the case with $Ri = 400$. The drag decreases as F decreases further from the largest F in regime II. Stein (1992) suggested that drag is influenced by three effects: (1) the increases in wave amplitude generated by a higher mountain, (2) a drag

Table 3. The nondimensional maximum wind speed at lee slope for different F and Ri. The cases for regime I, II, III, and IV are denoted as regular, bold, italicized, and bold italicized numbers, respectively

F \ Ri	20	100	400	900	infinity ($\alpha = 0$)	900^- ($\alpha < 0$)	400^- ($\alpha < 0$)
1.2	1.36	1.67	1.68	1.80	1.85	**2.32**	**2.36**
1.1	1.39	1.69	1.87	**2.09**	**2.56**	**2.51**	**2.40**
1.0	1.43	1.84	1.93	**2.87**	**2.65**	**2.53**	**2.50**
0.9	1.45	1.91	**3.03**	*2.93*	*2.66*	*2.69*	*2.66*
0.8	1.47	2.00	**3.03**	*3.08*	*3.02*	*2.80*	*2.80*
0.7	1.51	2.04	*3.22*	*2.96*	*3.15*	*3.01*	*2.88*
0.6	1.61	**3.41**	**3.76**	*3.20*	*3.46*	*3.05*	*3.02*
0.5	1.68	***4.50***	***3.93***	***3.28***	***3.42***	***2.92***	***3.02***

Table 4. The nondimensional drag for different F and Ri. The cases for regime I, II, III, and IV are denoted as regular, bold, italicized, and bold italicized numbers, respectively

F \ Ri	20	100	400	900	infinity ($\alpha = 0$)	900^- ($\alpha < 0$)	400^- ($\alpha < 0$)
1.2	0.39	1.23	1.41	1.48	1.15	**3.28**	**3.37**
1.1	0.38	1.12	1.62	**5.34**	**4.09**	**3.77**	**3.21**
1.0	0.35	1.25	1.58	**4.98**	**3.76**	**3.34**	**2.99**
0.9	0.35	1.27	**5.04**	*4.70*	*3.32*	*2.91*	*2.41*
0.8	0.32	1.25	**4.41**	*3.65*	*3.32*	*2.79*	*1.94*
0.7	0.31	1.22	*3.72*	*3.52*	*3.25*	*2.88*	*2.21*
0.6	0.41	**4.92**	***3.51***	*3.31*	*3.02*	*2.50*	*2.44*
0.5	0.50	***6.55***	***4.57***	***2.79***	***2.71***	***2.41***	***2.27***

amplification by the nonlinearities, and (3) the decrease of the active height of the mountain due to the blocked region that gives a lower force against the flow (Rottman and Smith, 1989). He explained the decrease in drag for lower F in a way that the third effect exceeds the other two for very high mountains and lowers the main exponent of the drag.

In this section, we find:

1) There are four flow regimes for vertically sheared flow over a two-dimensional mountain ridge similar to those proposed by LW for uniform flow. However, the critical F's which separate the flow regimes decrease by forward shear and increase by backward shear. The height of stagnation aloft is increased by forward shear and decreased by backward shear. 2) Linear theory is found to be able to predict the location of the stagnation aloft and capture the tendency of the modification of F_c for the occurrence of wave breaking by vertical shear. These findings will be applied to help explain an observed severe downslope wind storm in Sect. 5.

4. The effects of sharp gradients in static stability

a) Linear flow

In this section, we consider a two-layer atmosphere with uniform flow U and discontinuity in the Brunt-Väisälä frequency, with N_2 in the upper layer and N_1 in the lower layer. The height of the interface is at $z = z_1$. N_2 may be either larger or smaller than N_1. That is, λ_{12}, defined as N_2/N_1, may be either larger or smaller than 1. Adopting a linear lower boundary condition at $z = 0$, continuity of vertical velocity and perturbation pressure as interface conditions, and imposing a radiation upper boundary condition, the analytical solution for the horizontal wind perturbation can be obtained.

$$u_1'(x,z) = \frac{Uha\lambda_1}{a^2 + x^2} \times [a(\sin\lambda_1 z + 2c_r\cos\lambda_1 z) - x(2c_i - 1)\cos\lambda_1 z] \quad \text{for } z \le z_1,$$

$$u_2'(x,z) = \frac{Uha\lambda_2}{a^2+x^2} \times [(\cos\lambda_1 z_1 - 2c_r \sin\lambda_1 z_1) \times (a\sin\lambda_2(z-z_1) + x\cos\lambda_2(z-z_1)) + \sin\lambda_1 z_1 (2c_i - 1)(x\sin\lambda_2(z-z_1) - a\cos\lambda_2(z-z_1))] \quad \text{for } z > z_1, \tag{17}$$

where

$$\lambda_1 = \frac{N_1}{U}, \tag{18}$$

$$\lambda_2 = \frac{N_2}{U}, \tag{19}$$

$$c_r = \frac{(\lambda_{12}-1)\cos\lambda_1 z_1 \sin\lambda_1 z_1}{2(\cos^2\lambda_1 z_1 + \lambda_{12}\sin^2\lambda_1 z_1)}, \tag{20}$$

and

$$c_i = \frac{(1-\lambda_{12})(\cos^2\lambda_1 z_1 - \lambda_{12}\sin^2\lambda_1 z_1)}{2(\cos^2\lambda_1 z_1 + \lambda_{12}^2\sin^2\lambda_1 z_1)}, \tag{21}$$

where $\lambda_{12} = \lambda_2/\lambda_1 = N_2/N_1$. The comparison of the analytical solutions in Eq. (17) and those from the nonlinear numerical simulations are shown in Fig. 8 for cases with $F = U/N_1 h = 10$, $\lambda_{12} = 0.4$ or 2 (*i.e.*, $N_1 = 0.01\,\mathrm{s}^{-1}, N_2 = 0.004$ or $0.02\,\mathrm{s}^{-1}$, respectively), and $z_1 = 0.75\lambda_z$ where $\lambda_z = 2\pi U/N_1$. The depth of the lower layer (z_1) is taken as its nondimensional value in further discussions in this section. Figure 8a shows u' from Eq. (17) for the case with $\lambda_{12} = 0.4$. It is apparent that the vertical wavelength is larger in the upper layer where the Brunt-Väisälä frequency is smaller than that in the lower layer, since the vertical wavelength is $2\pi U/N_i$. The magnitude of u' in the upper layer is smaller than that in the lower layer. The corresponding w' (not shown) has a larger magnitude in the upper layer than that in the lower layer. This is due to over-transmission since the transmission coefficient is greater than one when there exists a less stable upper layer. The transmission coefficient as a function of λ_{12} will be shown later in this section. The vertical velocity w' in Fourier space is just proportional to the transmission coefficient. However, u' in Fourier space is proportional to not only the transmission coefficient but also λ_2. The relative magnitudes of u' in the upper layer compared to those in the lower layer may be determined by the net effects of the above two parameters. Figure 8b shows u' from the analytical solution for the case with $\lambda_{12} = 2$. Opposite to that shown in Fig. 8a, the vertical wavelength is smaller in the upper layer than that in the lower layer since there exists a more stable upper layer. However, the magnitudes of u' in the upper layer are about the same as those in the lower layer in this case. Figure 8c and d shows the corresponding nonlinear numerical simulations to those shown in Fig. 8a and b, respectively. The basic features are similar in such a highly linear case ($F = 10$), especially the flow responses in the lower layer. The magnitudes of u' in the upper layer from numerical simulation are relatively smaller than those predicted by linear theory. The differences may be due to the numerical diffusion and the influence of the upper boundary condition as indicated in LW. Since F is fairly large in this case, nonlinearity does not play an important role. The analytical and numerical results agree well. Durran (1986) suggests the nonlinear effects become significant when the stability has a multi-layer structure. We will discuss the nonlinear cases later in this section.

Our interests in this section are the general effects of sharp gradients in static stability on the two-dimensional, nonrotating orographically-forced flow response. Therefore we calculate the strongest horizontal wind speed on the lee slope ($U_{\max}$), the smallest horizontal wind speed on the upslope surface ($U_{\min}$), the reflection coefficient (Ref), and the transmission coefficient (Tran) for different combinations of λ_{12} and z_1. $U_{\max}$ and $U_{\min}$ can be obtained using the same approach as that in Sect. 3 to obtain Eqs. (15) and (16). The reflection and transmission coefficients can be calculated during the process of solving the analytical solution of Eq. (17), they are

$$\mathrm{Ref} = \frac{|1-\lambda_{12}|}{1+\lambda_{12}}, \tag{22}$$

$$\mathrm{Tran} = \frac{2}{1+\lambda_{12}}. \tag{23}$$

Ref (Tran) is defined as the squared ratio of the downward (upward) propagating wave amplitude in the lower (upper) layer to that of the upward component in the lower layer.

Figure 9a shows $U_{\max}$ (normalized by basic wind speed) in $z_1 - \log(\lambda_{12})$ parameter space for

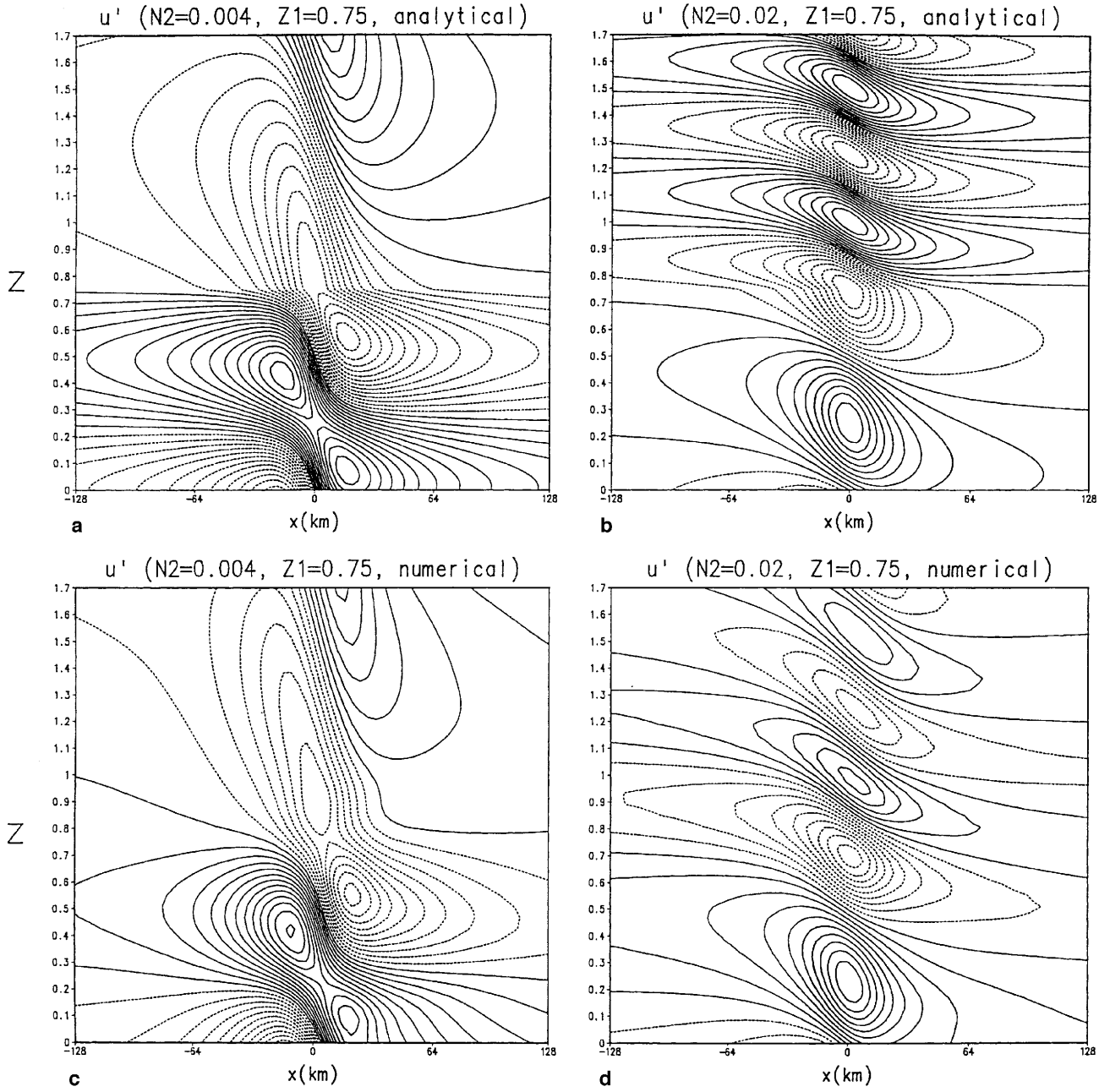

Fig. 8. **a** The horizontal perturbation wind field in a two-layer atmosphere from the analytical solution of Eq. (17) with $F = 10$, $z_1 = 0.75$, and $\lambda_{12} = 0.4$ (i.e., $N_1 = 0.01\,\mathrm{s}^{-1}$, and $N_2 = 0.004\,\mathrm{s}^{-1}$); **b** same as in **a** except for $\lambda_{12} = 2$; **c** Same as in **a** except from a nonlinear numerical simulation; **d** same as in (c) except for $\lambda_{12} = 2$

cases with $F = 10$. $\log(\lambda_{12}) < 0$ when $\lambda_{12} < 1$ and $\log(\lambda_{12}) > 0$ when $\lambda_{12} > 1$. It is obvious that the largest $U_{\max}$ occurs in the case with $\log(\lambda_{12}) = -2$ when z_1 is near $0.25 + n/2$ or in the case with $\log((\lambda_{12}) = 2$ when z_1 is near $n/2$, where $n = 0, 1, 2, \ldots$. The magnitude of the largest $U_{\max}$ for a certain $\log(\lambda_{12})$ is proportional to the absolute value of $\log(\lambda_{12})$. Figure 9b shows the variation of $U_{\max}$ with $\log(\lambda_{12})$ for those cases with $z_1 = 0.255$ and $z_1 = 0.505$. For cases with $z_1 = 0.255$, $U_{\max}$ decreases from about 2.48 to 1.0 as $\log(\lambda_{12})$ increases from -2 to 2. The variation of $U_{\max}$ for cases with $z_1 = 0.505$ is totally opposite of that for cases with $z_1 = 0.255$. $U_{\max}$ increases from about 1.0 to 2.48 as $\log(\lambda_{12})$ increases from -2 to 2. Notice that when $U_{\max} =$

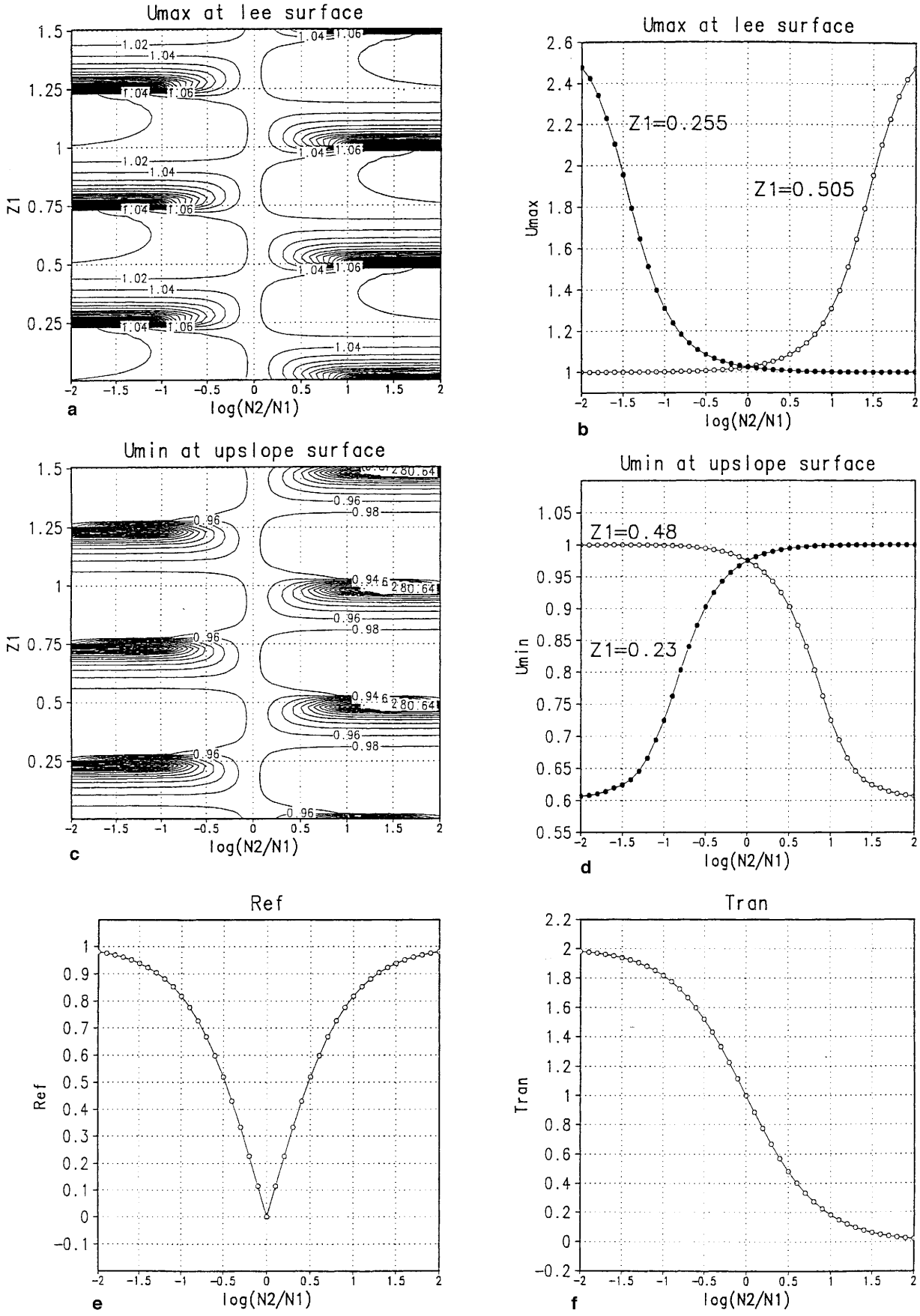

Fig. 9. **a** The strongest horizontal wind speed at the lee surface from analytical solution for a two-layer atmosphere. **b** The variation curves for the cases with $z_1 = 0.255$ and 0.505 in **a**; **c** Same as in **a** except for the smallest horizontal wind speed at upslope surface; **d** The variation curves for the cases with $z_1 = 0.23$ and 0.48 in **c**; **e** The reflection coefficient as a function of $\log(\lambda_{12})$ from the analytical solution. **f** Same as in **e** except for the transmission coefficient

2.48, the response can be classified as a severe downslope wind. For cases with smaller $|\log(\lambda_{12})|$, the location of z_1 with largest $U_{\max}$ for that particular $\log(\lambda_{12})$ is a little different from that for cases with $\log(\lambda_{12}) = -2$ or 2. For example, the location of z_1 with largest $U_{\max}$ is near $0.3 + n/2$ when $\log(\lambda_{12}) = -0.1$ and is near $0.05 + n/2$ when $\log(\lambda_{12}) = 0.1$.

Figure 9c shows $U_{\min}$ (normalized by U) in $z_1 - \log(\lambda_{12})$ space for cases with $F = 10$. The smallest $U_{\min}$ occurs in the case with $\log(\lambda_{12}) = -2$ when z_1 is near $0.255 + n/2$, or in the case with $\log(\lambda_{12}) = 2$ when z_1 is near $n/2$. Again, for cases with smaller $|\log(\lambda_{12})|$, the location of z_1 with smallest $U_{\min}$ for that particular $\log(\lambda_{12})$ is a little different from that for cases with $\log(\lambda_{12}) = -2$ or 2. For example, the location of z_1 with smallest $U_{\min}$ is near $0.2 + n/2$ when $\log(\lambda_{12}) = -0.1$ and is near $0.45 + n/2$ when $\log(\lambda_{12}) = 0.1$. The magnitude of the smallest $U_{\min}$ decreases as the absolute value of $\log(\lambda_{12})$ increases. Figure 9d shows the variation of $U_{\min}$ with $\log(\lambda_{12})$ for cases with $z_1 = 0.23$ and $z_1 = 0.48$. For cases with $z_1 = 0.23$, $U_{\min}$ increases from about 0.61 to 1.0 as $\log(\lambda_{12})$ increases from -2 to 2. The variation of $U_{\min}$ for cases with $z_1 = 0.48$ is totally opposite of that for cases with $z_1 = 0.23$. $U_{\min}$ decreases from about 1.0 to 0.61 as $\log(\lambda_{12})$ increases from -2 to 2. Upstream blocking occurs when $U_{\min} < 0$. Therefore, this may imply that *the possibility of upstream blocking increases by decreasing* λ_2 *in cases with* $\log(\lambda_{12}) < 0$ *and* z_1 *near* $0.25 + n/2$, *or by increasing* λ_2 *in cases with* $\log(\lambda_{12}) > 0$ *and* z_1 *near* $n/2$.

Figure 9e and f show the Ref and Tran, respectively, as functions of $\log(\lambda_{12})$. Notice that both Ref and Tran are not functions of z_1, according to Eqs. (22) and (23). It is apparent that Ref is symmetric with $\log(\lambda_{12}) = 0$, i.e. Ref is a function of $|\log(\lambda_{12})|$. Ref decreases from 0.98 to 0 when $\log(\lambda_{12})$ increases from -2 to 0, and then increases from 0 to 0.98 when $\log(\lambda_{12})$ further increases from 0 to 2. However, Tran decreases from 1.98 to 0.02 when $\log(\lambda_{12})$ increases from -2 to 2. When $\log(\lambda_{12}) = 0$, i.e. $N_2 = N_1$, Tran = 1. The large Ref in cases with $\log(\lambda_{12}) = -2$ and 2 may explain the occurrence of largest $U_{\max}$ and smallest $U_{\min}$ in such cases when z_1 is located at an optimal height as shown in Fig. 9a and c.

One may be curious about whether the linear theory results shown in Fig. 9 are applicable when nonlinearity is taken into consideration. Figure 10a and b shows the comparison between $U_{\max}$ obtained from both analytically and numerically for $F = 10, N_1 = 0.01\,\mathrm{s}^{-1}, 0 < z_1 < 1.5$, and $N_2 = 0.004\,\mathrm{s}^{-1}$ (i.e., $\lambda_{12} = 0.4$; Fig. 10a) or $0.02\,\mathrm{s}^{-1}$ (i.e., $\lambda_{12} = 2$; Fig. 10b). As indicated in Fig. 9, $U_{\max}$ from the analytical solution oscillates with z_1 and repeats its value every 0.5 when F and λ_{12} are fixed. Basically, this oscillation in the analytical solution is supported by nonlinear numerical simulation results for cases with $F = 10$, although there is a slight difference in the magnitudes. The largest $U_{\max}$ occurs when z_1 is near 0.3, 0.8, or 1.3 in Fig. 10a. On the other hand, for cases with $\lambda_{12} = 2$ (Fig. 10b), the largest $U_{\max}$ occurs when z_1 is near 0.05, 0.55 and 1.05 where the trough of the $U_{\max}$ curve is observed in such locations of z_1 for cases with $\lambda_{12} = 0.4\,\mathrm{s}^{-1}$ (Fig. 10a). In other words, the curves in Fig. 10a and b are almost totally out of phase. The corresponding drag (normalized by $\rho\pi U N_1 h^2/4$) based on numerical simulations in Fig. 10a and b is shown in Fig. 10c and d, respectively. It is apparent that there exists an in-phase property between the curves of $U_{\max}$ and drag. The drag from highly nonlinear cases will be investigated in the next subsection to check if this in-phase property still exists when the nonlinearity is strong.

b) Nonlinear flow

The cases shown in Fig. 10 are very linear and therefore the nonlinearity does not play an important role in the flow response. The real atmosphere may be strongly nonlinear, especially when wave breaking occurs. Whether linear theory can be applied may have to be carefully checked for such cases. Wave breaking has been found to be necessary for severe downslope winds to occur (Clark and Peltier, 1984; Smith, 1985). Here we discuss the nonlinear numerical responses. The linear theory in the previous subsection at least gives us a clear indication that both, the interface height and the ratio λ_{12}, are important in influencing the flow behavior.

In order to investigate the nonlinear problem, we use the numerical model described in Sect. 2. Almost all numerical models adopted to study

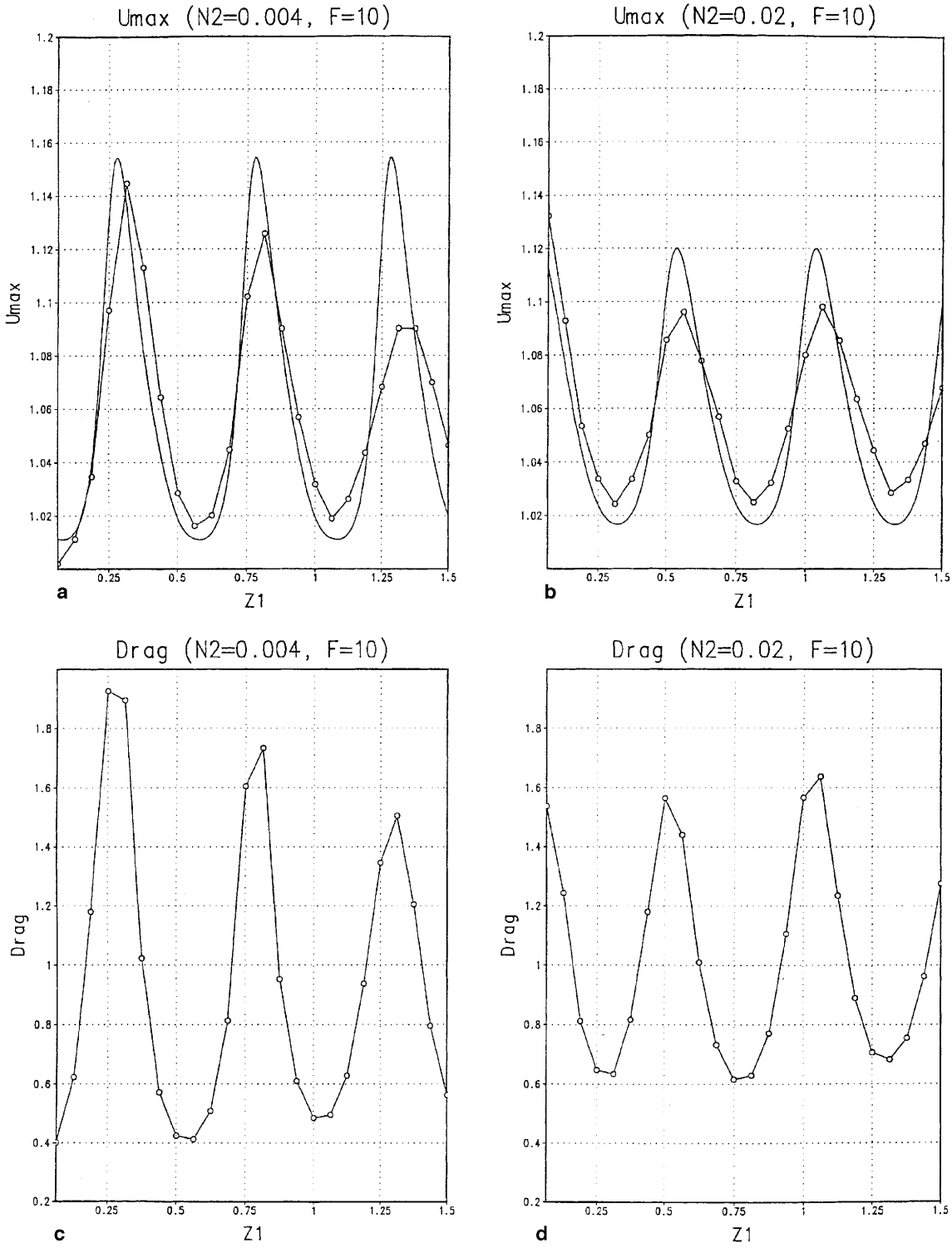

Fig. 10. The comparison of strongest horizontal wind speed (normalized by U) at the lee surface from linear theory (solid line) and nonlinear numerical solutions (line with circles) for the cases with $F = 10$ and (a) $\lambda_{12} = 0.4$, (b) $\lambda_{12} = 2$

mountain problems involve a transformation from Cartesian to a terrain-following coordinate system, the one used here is without exception. The most popular transformation is that proposed by Gal-Chen and Somerville (1975) who define the terrain-following coordinate $\sigma = z_T(z - z_s)/(z_T - z_s)$, where $z_s(x)$ is the mountain geometry and z_T is the top of computational domain. The

governing equations in such a model are actually calculated in (x, σ) space instead of (x, z) space. Therefore, the effects of coordinate transformation may have to be taken into consideration when a (x, z) space linear theory is applied to interpret the (x, σ) space numerical results. For example, linear theory applies the lower boundary condition at $z = 0$ and predicts that there exists the strongest low-level response at some certain z_1 for flow over mountain in a two-layer atmosphere as shown in Fig. 9a. These values of z_1 should be interpreted as values of σ_1 in an (x, σ) coordinate system, since the lower boundary condition is applied at $\sigma = 0$ in such a system. In the following, these effects will be considered and the value of σ_1 is used as a control parameter. However, we still use the symbol z_1, which makes the results easier to compare with linear theory.

A large number of systematic nonlinear numerical simulations are conducted to investigate the effects of two-layer structured atmospheric flow over an isolated mountain ridge. Figure 11 shows the normalized surface drag, which provides a good measure of the strength of the wave response, as a function of z_1. Figure 11a shows the drag for cases with $F = 1.5$ and $\lambda_{12} = 0.4$. If we define a high-drag state, based on the simulated flow structure, as those with surface drag greater than 2, it is found that the high drag state occurs in cases with $z_1 = 0.25$, $0.3125, 0.375, 0.6875, 0.75, 1.375$, and 1.4375. Notice that $F = 1.5$ is characterized as a low-drag state if U and N are both constant with height, according to LW or Long's nonlinear theory. Therefore, we may consider those high-drag state cases in Fig. 11a as "tuned" by the structured atmosphere. Comparing the drag curve in Fig. 11a with that of $U_{\max}$ in Fig. 10a, it can be seen that these two curves have similar tendencies in the locations of the crests and troughs. At values of z_1 where there exist relatively large $U_{\max}$ in Fig. 10a, there is also found a relatively large surface drag in Fig. 11a. This implies that linear theory may be used to predict the possibility of high-drag state flow, to a first approximation.

Figure 11b shows the drag for cases with $F = 1.2$ and $\lambda_{12} = 0.4$. In these cases, F is very close to the critical value (1.18) of the high-drag state which is predicted for cases with uniform U and N (Miles and Huppert, 1969). Compared to the results in Fig. 11a, more cases can be characterized as high-drag states in addition to those found in Fig. 11a. However, the curve still has the similar tendency to that predicted by linear theory (Fig. 10a). Figure 11c shows the drag for cases with $F = 1.0$ and $\lambda_{12} = 0.4$. For such F, all cases except the one with $z_1 = 0.0625$ are high-drag state flows. Again, the curve has a similar tendency to that predicted by linear theory (Fig. 10a), except for $z_1 > 1$. Notice that $F = 1.0$ is located in regime II for a high-drag state flow in the case with uniform U and N according to LW.

According to the results in Fig. 11a–c, we find that F_c depends on the location of z_1 if a certain λ_{12} is considered. For example, the critical F in cases with $z_1 = 0.0625$ must be some value less than 1, since a high-drag state flow is not observed even when $F = 1.0$, although the drag increases from 1.2 to 1.7 when F decrease from 1.5 (Fig. 11a) to 1.0 (Fig. 11c). For cases with $z_1 = 0.25$, the critical F is found to lie between 1.2 and 1.5 since the high-drag state is observed in the case with $F = 1.2$ (Fig. 11b) and not in that with $F = 1.5$ (Fig. 11a). F_c for cases with $z_1 = 0.375$ is some value greater than 1.5, since high-drag states are observed in cases with $F = 1.5$, 1.2, and 1.0. The range in which F_c may be located in cases with other z_1 can be obtained using the same analysis as above. However, the exact value of F_c for different z_1 may be practically difficult to obtain numerically, since it requires an intensive number of simulations. In addition, F_c is different for different λ_{12}. Nevertheless, we may still conclude that *the F_c for a high-drag state is larger when z_1 is located near $0.3 + n/2$ than that when z_1 is located near $0.05 + n/2$ if there exists a less stable upper layer* $(e.g., \lambda_{12} = 0.4)$, according to the results from Fig. 11a–c.

Figures 11d–f shows the drag obtained from numerical simulations with the same parameters as those in Fig. 11a–c, respectively, except with $\lambda_{12} = 2$. The curves in Fig. 11d–f have similar tendencies as those predicted by linear theory (Fig. 10b), with crests occurring when z_1 is near $0.05 + n/2$ and troughs when z_1 is near $0.3 + n/2$. The range of F_c for certain z_1 can be obtained from the values of drag for different F using the similar analysis as before. F_c is less than 1 for cases with $z_1 = 0.75$, 0.8125, 0.875, and 0.9375, since these cases are characterized as

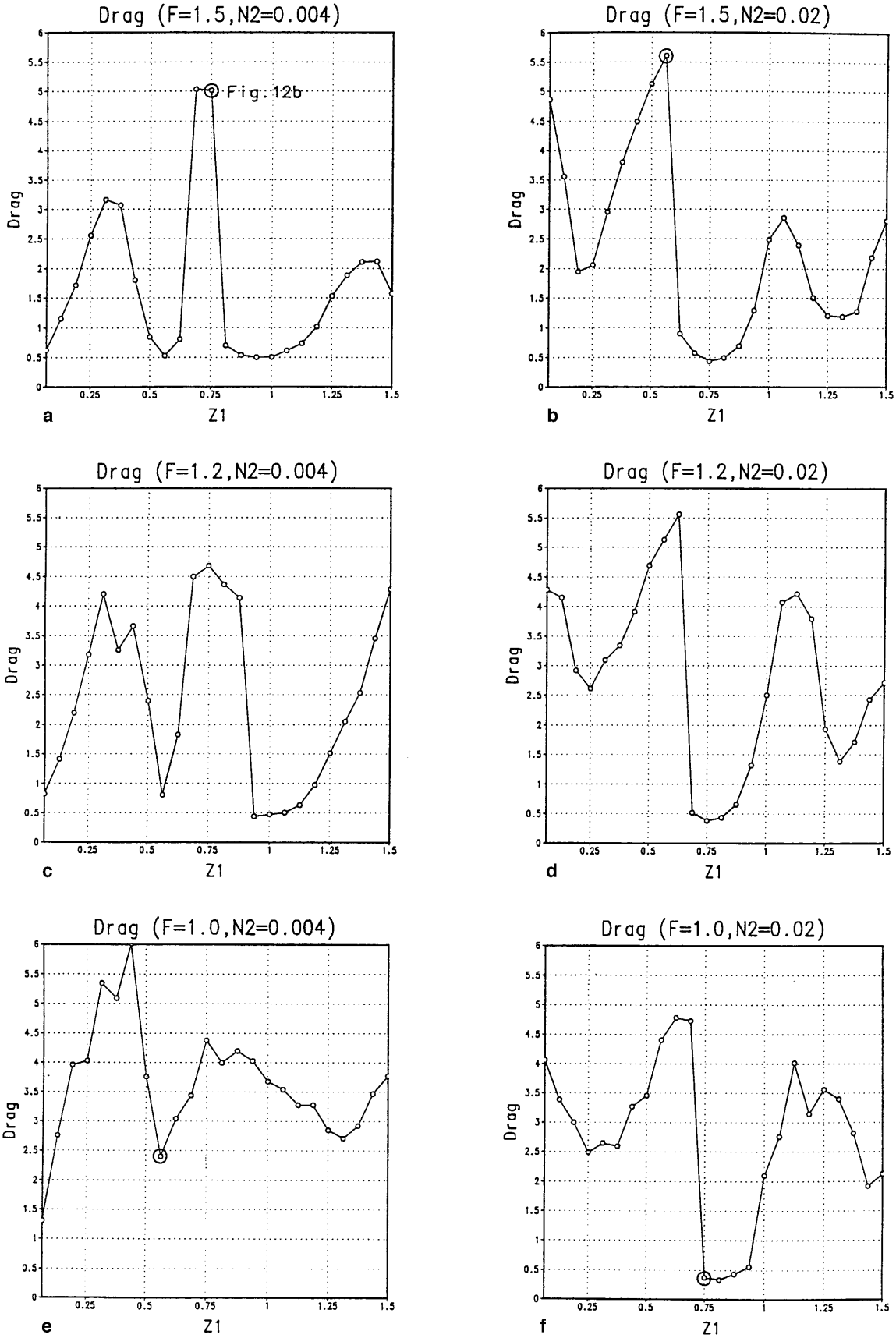

Fig. 11. The normalized surface drag from a nonlinear numerical simulations for the cases with $(F, \lambda_{12}) =$: **a** (1.5, 0.4), **b** (1.2, 0.4), **c** (1.0, 0.4), **d** (1.5, 2), **e** (1.2, 2), and **f** (1.0, 2)

low-drag state flows when $F = 1.0$ (Fig. 11f). This means that these cases are strongly "detuned" by the structured atmosphere since $F = 1$ is located in a high-drag state regime for the uniform U and N case. We may conclude that *the F_c for a high-drag state is larger when z_1 is located near $0.05 + n/2$ than that when z_1 is located near $0.3 + n/2$ if there exists a more stable upper layer* (*e.g.*, $\lambda_{12} = 2$), according to the results from Fig. 11d–f.

From the above analysis, we find the similarity between the curves of U_{max} (Fig. 10a, b) from linear theory and the curves of drag (Fig. 11) from nonlinear numerical simulations. This similarity implies that $U_{\max}$ in $z_1 - \log(\lambda_{12})$ space shown in Fig. 2a may be very useful in the qualitative analysis of the possibility of high-drag state flows in different situations. We find that when linear theory predicts a larger $U_{\max}$, the possibility of a high-drag state in the nonlinear numberical simulation is also enhanced. In other words, the F_c is larger in cases with larger $U_{\max}$ predicted by linear theory. According to the results shown in Fig. 9a, even the case with very large F can be characterized as a high-drag state flow when $\log(\lambda_{12}) = -2$ and z_1 is near $0.25+ n/2$, or when $\log(\lambda_{12}) = 2$ and z_1 is near $n/2$. However, such cases may be of academic interest only, since N_2 in the upper layer which extends to infinity has never been so small ($0.0001\ \mathrm{s}^{-1}$) or so large ($1.0\ \mathrm{s}^{-1}$). The most realistic case in the atmosphere may be the one with $\log(\lambda_{12})$ between 0 to 0.5, which is usually applied to simulate the stratosphere as a more stable upper layer.

In order to get further detailed information about the flow behavior when "tuned" or "detuned" effects exist, the horizontal wind fields are plotted in Fig. 12 for certain cases. Figure 12a and d shows the horizontal wind field for cases with $F = 1.5$ and 1.0, respectively, when U and N are both uniform with height as control cases. Figure 12b, c, e, and f shows the horizontal wind fields for the cases marked in Fig. 11. The purpose of Fig. 12 is to show the "tuned" and "detuned" effects on the flow response in a two-layer atmosphere. Figure 12a shows that the flow behavior has features of typical linear mountain waves without severe downslope winds. However, if there exists a less stable layer $\lambda_{12} = 0.4$ located at $z > 0.75\lambda_z$ (Fig. 12b), or a more stable layer $\lambda_{12} = 2$ located at $z > 0.5625\lambda_z$ (Fig. 12c), strong downslope winds may be triggered due to the partial reflection from the upper layer for such a fairly large F. These results may be viewed as numerical evidence of "tuned" effects in a two-layer atmosphere. On the other hand, Fig. 12d shows that when $F = 1.0$, there exists a high-drag state flow with strong downslope winds for the case with uniform U and N. However, if there exists a less stable layer $\lambda_{12} = 0.4$ located at $z > 0.5625\lambda_z$ (Fig. 12e), or a more stable layer $\lambda_{12} = 2$ located at $z > 0.75\lambda_z$ (Fig. 12f), strong downslope winds may be significantly suppressed or even eliminated due to partial reflection from the upper layer. These results provide the numerical evidence of "detuned" effects.

Durran (1986) provided numerical results with "tuned" effects for cases with $F > 1.2$. However, he suggested that in some cases the amplification of the linear solution produced by the layered structure disappears when the flow is nonlinear, while in other cases the damping associated with the linear wave gives way to very strong amplification in the nonlinear regime, according to his Table 1 and Fig. 1. We find part of the reason for that is from the neglect of the coordinate transformation in calculating the interface height. Besides, linear theory should not be expected to predict the exact F_c for the occurrence of high-drag states even in an unstructured atmosphere.

As aforementioned, wave breaking requires the existence of stagnation aloft. Adopting the similar method in previous section, we can obtain the u' profile at $x = 0$. In order to find the minimum of $u'(0, z)$, one has to take vertical derivative of $u'(0, z)$ in both layers, and the locations of extreme u' can be calculated by making the derivative equal to 0. After the calculations, the heights (normalized by $2\pi U/N_1$) with minimal u' in both the lower and upper layers are obtained from Eq. (17)

$$z_{1c} = \frac{\pi + \tan^{-1}\frac{1}{2c_r}}{2\pi}, \tag{24}$$

and

$$z_{2c} = \frac{\pi + \tan^{-1}\left[\dfrac{2c_r \sin\lambda_1 z_1 - \cos\lambda_1 z_1}{(2c_i - 1)\sin\lambda_1 z_1}\right]}{2\pi}, \tag{25}$$

respectively. From the results of uniform or forward shear flow, we know that the first stage

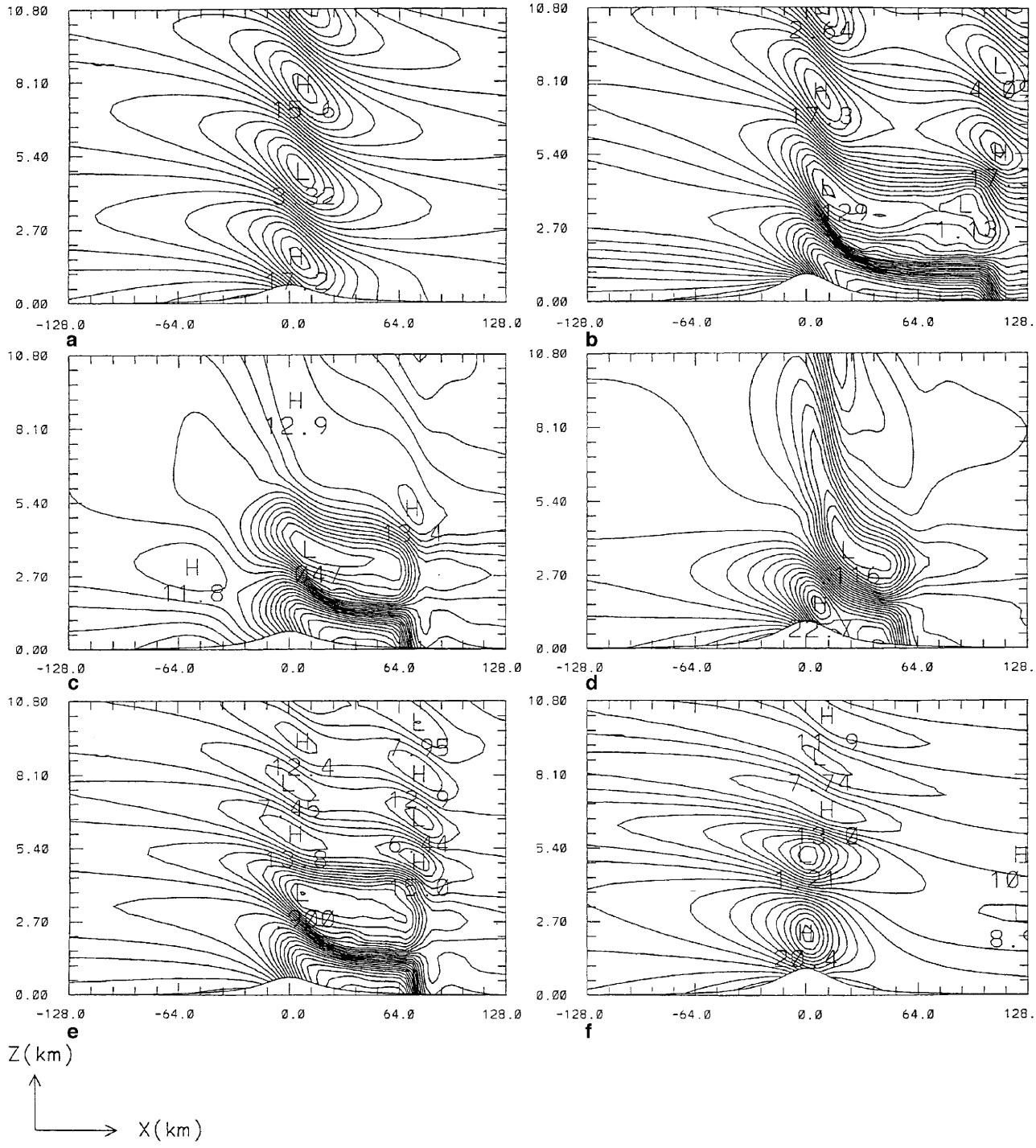

Fig. 12. The horizontal wind field from a nonlinear numerical simulations for the cases with **a** $F = 1.5$, $\lambda_{12} = 1$; **b** $F = 1.5$, $\lambda_{12} = 0.4$, $z_1 = 0.75$; **c** $F = 1.5$, $\lambda_{12} = 2$, $z_1 = 0.5625$; **d** $F = 1.0$, $\lambda_{12} = 1$; **e** $F = 1.0$, $\lambda_{12} = 0.4$, $z_1 = 0.5625$; and **f** $F = 1.0$, $\lambda_{12} = 2$, $z_1 = 0.75$

in the development of severe dewnslope winds is the existence of stagnation at the second phase of the u' field of the wave (Scinocca and Peltier, 1993). The stagnation aloft is found to occur near 0.75 vertical wavelength when both U and N are uniform (Clark and Peltier, 1984; Laprise and Peltier, 1989). In the two-layer structured atmosphere considered in this study, U and N are uniform in each layer. Therefore, we assume that stagnation occurs in the upper layer in cases with

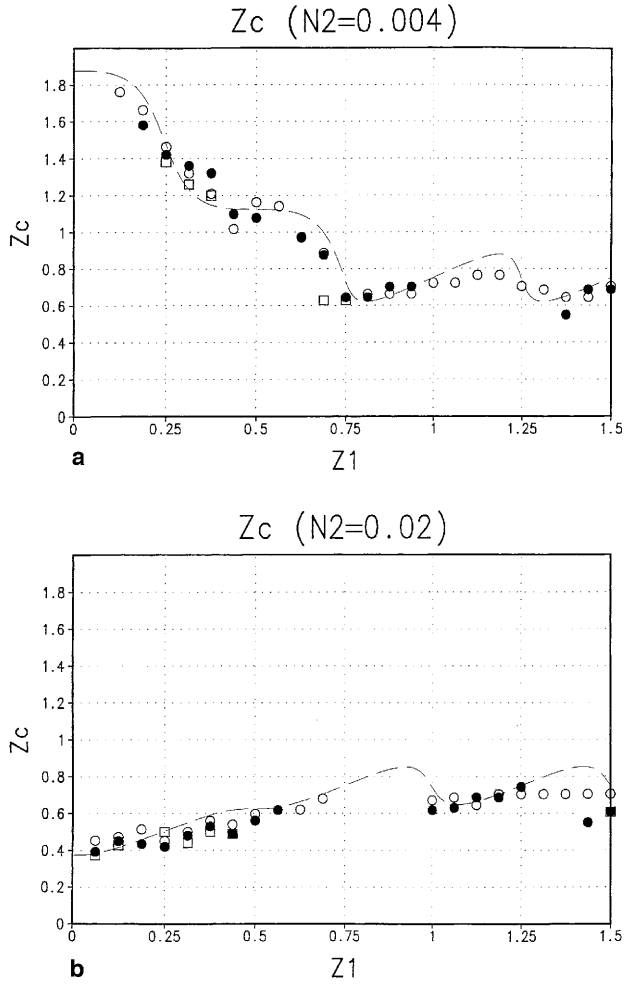

Fig. 13. The nondimensional initial overturning level (z_c) from nonlinear numerical simulations for the cases shown in Fig. 11 with **a** $\lambda_{12} = 0.4$, **b** $\lambda_{12} = 2$. Open circles denote the cases with $F = 1.5$, close circles with $F = 1.2$, and open square with $F = 1.0$. The dash lines represent the corresponding results from linear theory

$z_1 < 0.75$, while it occurs in the lower layer if $z_1 > 0.75$, that is, $z_c = z_{2c}$ if $z_1 < 0.75$ and $z_c = z_{1c}$ if $z_1 > 0.75$.

Figure 13 shows the comparison of z_c from Eqs. (24) and (25) and the nondimensional height for the first detection of stagnation aloft from our nonlinear numerical simulations shown in Fig. 11. Values of z_c from linear theory is plotted as a dashed line in Fig. 13. In cases with $\lambda_{12} = 0.4$, z_c decreases from 1.875 to 0.75 as z_1 increases from 0 to 0.75 while it starts to oscillate with the center at $z_c = 0.75$ when $z_1 > 0.75$. In cases with $\lambda_{12} = 2$, z_c increases from 0.375 to 0.75 as z_1 increases from 0 to 0.75 and it starts to oscillate with the center at $z_c = 0.75$ when $z_1 > 0.75$. The larger (smaller) z_c in cases with $\lambda_{12} = 0.4(2)$ when $z_1 < 0.75$ is due to the larger (smaller) local vertical wavelength in the upper layer than that in the lower layer as indicated in Fig. 8. The heights where the stagnation aloft is first detected from the nonlinear numerical simulation are also plotted in Fig. 13. They are found to agree very well with those predicted by linear theory. Therefore, we may conclude that *linear theory gives a good prediction of the location of stagnation aloft*.

In conclusion, we find that *linear theory is very useful in predicting the level of stagnation aloft* (z_c) *and in qualitative analysis of the possibility of high-drag state flow in a two-layer atmosphere*. We will use the findings in this and previous sections to investigate an observed severe downslope windstorm, in which there exists both shear and multi-layer stability in the sounding, in the next section.

5. The severe windstorm of 11 January 1972 in Boulder

The observational data for the severe windstorm which occurred in Boulder, Colorado, on 11 January 1972 have been discussed many times (e.g., Lilly and Zipser, 1972; Klemp and Lilly, 1975; Lilly, 1978; Peltier and Clark, 1979; Durran, 1986). The data for this case are the most well-documented of any published case study concerning the height variations of the structure of the wave field. The background wind and temperature profiles which were obtained from the Grand Junction sounding upstream of Boulder during the windstorm are shown in Fig. 18 of Peltier and Clark (1979). The wind speed increases linearly from $10\,\mathrm{ms}^{-1}$ at the surface to $50\,\mathrm{ms}^{-1}$ at $z = 10\,\mathrm{km}$ and then decreases from $50\,\mathrm{ms}^{-1}$ at $z = 10\,\mathrm{km}$ to $20\,\mathrm{ms}^{-1}$ at about $z = 12\,\mathrm{km}$, above which it is constant. In the temperature profile, there exists an inversion between 2.7 and 4.7 km and an isothermal layer for $z > 10\,\mathrm{km}$. Klemp and Lilly (1975) emphasized the fundamental role of the inversion layer in generating a large-amplitude response in their linear theory. They suggested that this strong amplification is associated with partial reflection of upward propagating wave energy by variations in thermal stability. Durran (1986) indicated that if this inversion is removed from the upstream

sounding, no windstorm develops, according to his numerical simulation. He also found that when the inversion is retained, but the change in atmospheric structure at the tropopause is eliminated, a significant windstorm still develops.

Considering this observed wind profile for the Boulder severe downslope windstorm, *Ri* is about 6.25 ($\alpha = 0.004$, N is about $0.01\,s^{-1}$) for $z < 10\,km$. The surface wind speed in that profile is $10\,ms^{-1}$ and the mountain peak of the topography west of Boulder is about 2 km. Hence, F is about 0.5. According to the flow regime shown in Fig. 3a, it is located in regime I without the occurrence of wave breaking and there should be no strong downslope wind if N is constant with height. Therefore, the variation of stability may play an essential role in this observed windstorm.

In this section, we use these observational wind velocity and temperature profiles as the initial data for our numerical model to investigate the mechanism of partial reflection. Figure 14a shows the simulated potential temperature field at $t = 12000\,s$. It is apparent that the internal jump forms and propagates downstream. The largest horizontal wind speed on the lee surface is $56\,ms^{-1}$ (not shown), which is very close to the value observed in this windstorm (Lilly, 1978). This figure should be compared with Fig. 10 of Durran (1986). The basic features of the severe downslope wind structure is similar except that there is no lee wave in our results since we use a hydrostatic model. However, Durran (1986) also suggested that the lee waves play no fundamental role in the development of strong downslope winds, as demonstrated from his simulations with a hydrostatic version of the model. Figure 14b shows the potential temperature field for the identical initial parameters as those in Fig. 14a except that the inversion between 2.7 and 4.7 km is removed from the initial sounding. Again, the results are consistent with Durran's study, and no windstorm develops in this case. The largest wind speed on the lee surface is about $35\,ms^{-1}$. The above two simulations show the capability of our model to reproduce the basic structure of the observational windstorm, and show good agreement with the results of other numerical studies.

According to the linear theory developed in the last section, the low-level response is not only a function of λ_{12} but also function of the location of interface (z_1). Although there are more layers in this static stability profile, we believe that the height of the interface still plays important role in the flow response. To verify this hypothesis, we conduct a simulation with the inversion located in a higher layer between 6.7 and 8.7 km. The result is shown in Fig. 14c. We find that no severe downslope winds exist when the inversion is located at such a level. According to linear theory for a two-layer system with uniform basic wind, "tuned" effects occur when z_1 is near $0.05 + n/2$ vertical wavelength and "detuned" effects occur when z_1 is near $0.3 + n/2$ vertical wavelength if λ_{12} is much larger than 1 (Fig. 9a). Since the local vertical wavelength varies with height when there exists shear in the wind profile, the optimal location of z_1 for "tuned" or "detuned" effects to occur in such cases becomes difficult to calculate. However, we may still analyze these processes to a first approximation. For the case in Fig. 14a, the interface for the lowest two layers is located at $z = 2.7\,km$ and the mountain height is 2 km. The nondimensional interface height above the mountain peak is about 0.04 times the averaged vertical wavelength in terrain-following coordinates if the mean vertical wavelength is calculated from averaged U ($30\,ms^{-1}$) and N ($0.01\,s^{-1}$) at $z < 10\,km$. Using the similar analysis, the interface in Fig. 14c is at about 0.25 mean vertical wavelength. Therefore, these results may be viewed as evidence of a partial reflection mechanism which may either enhance or suppress the possibility of wave breaking. Details depend on the location of the interface in a structural atmosphere.

To further verify the partial reflection mechanism, we remove the inversion from the sounding and place a less stable layer ($0.001\,s^{-1}$) between 9.7 and 11.7 km (Fig. 14d). We find that a severe downslope wind develops under this condition, although it develops at a later time as compared to the case shown in Fig. 14a. The interface above the mountain peak between this less stable layer and the lower layer is about 0.4 mean vertical wavelength in terrain-following coordinates. Notice that this interface height is close to the optimal z_1 for "tuned" effects to occur in a two-layer system, as shown in Fig. 9a. Thus, these results verify the partial reflection mechanism and provides an alternative condition for the development of severe downslope windstorms without the existence of a low-level inversion.

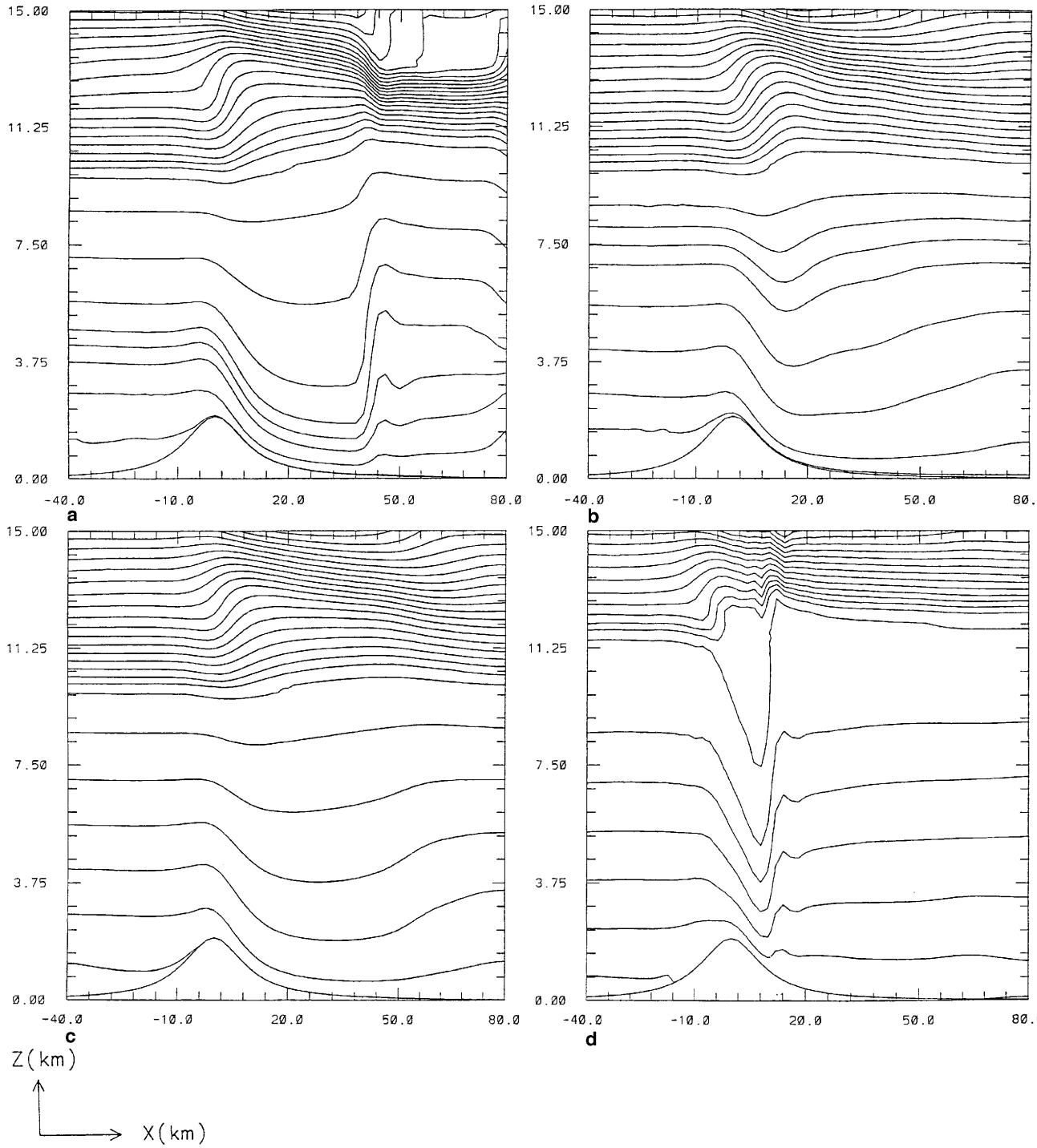

Fig. 14. a The potential temperature field from a nonlinear simulation of the 11 January 1972 Boulder windstorm using the upstream conditions observed at Grand Junction, at a model time 12000 s; **b** same as in **a**, except the inversion has been removed from the upstream sounding; **c** same as in **a**, except the inversion has been moved to a higher layer between $z = 6.7$ and $z = 8.7$ km; **d** same as in **b**, except a less stable layer has been added in the layer between $z = 9.7$ and $z = 11.7$ km

6. Concluding remarks

We have investigated the effects of shear and sharp gradients in static stability and demonstrated how a mountain wave and its associated surface winds can be strongly influenced. The linear theory for flow over an isolated mountain ridge with forward shear and constant static

stability shows that the horizontal wind speeds along both the lee and upslope surfaces are suppressed by forward shear. The critical $F(F_c)$ for the occurrence of wave breaking decreases when the strength of the forward shear increases, while the location for the wave-induced critical level is higher in cases with larger forward shear. This linear theory is then verified and interpreted by analyzing systematic nonlinear numerical results. Four flow regimes similar to those proposed by LW are also found for forward shear flow. However, the values of critical F which separate the flow regimes are lower when the strength of the forward shear is larger. The locations of stagnation aloft (wave-induced critical level) from numerical simulations are found to be quite consistent with those predicted by linear theory.

In considering the effects of two-layer stability, the strongest horizontal wind speed on the lee slope ($U_{\max}$), the smallest horizontal wind speed on the upslope surface ($U_{\min}$, the reflection coefficient (Ref), and the transmission coefficient (Tran) for different combinations of λ_{12} and z_1 are calculated from linear theory. Both Ref and Tran are found to be functions of the value of $\log(\lambda_{12})$, but not the interface height (z_1). Ref is larger when λ_{12} is much different from 1, no matter whether λ_{12} is larger or smaller than 1. However, Tran decreases when $\log(\lambda_{12})$ increases and approaches 0 when $\log(\lambda_{12})$ is large. The magnitude of the largest $U_{\max}$ (smallest $U_{\min}$) increases (decreases) as $|\log(\lambda_{12})|$ increases. It is found that the largest $U_{\max}$ occurs when z_1 is near $0.25 + n/2$ for cases with a less stable upper layer, or when z_1 is near $n/2$ for cases with a more stable upper layer. These results are confirmed by nonlinear numerical simulations. We find that linear theory is very useful in qualitative analysis of the possibility of high-drag state for different stability profiles. The locations of stagnation aloft in a two-layer atmosphere from numerical simulations agree very well with those predicted by linear theory.

The above findings are applied to investigate the Boulder severe downslope windstorm of 11 January 1972. We find that the windstorm cannot develop if the near mountain-top inversion is located at a higher altitude. However, if there exists a less stable layer right below the tropopause, the windstorm can develop without the existence of the low-level inversion. These results indicate the importance of partial reflection due to the structured atmosphere in influencing the occurrence of severe downslope windstorms, although partial reflection may not be the responsible mechanism for the generation of windstorms.

This study provides systematic numerical simulations to discuss how the flow regime is modified by wind shear and sharp gradients in static stability. Linear theory is proved to be very useful, in some sense, even in the nonlinear flow regime. The information from this study may be useful for improving the prediction of severe downslope windstorms.

Acknowledgements

This work is partially supported by the NSF Grant ATM-9224595. Discussions and comments on the manuscript by Drs. G. S. Janowitz, M. L. Kaplan, S. E. Koch, and R. P. Weglarz are highly appreciated. Part of the computations was performed on the CRAY Y-MP at the North Carolina Supercomputer Center.

References

Asselin RA (1972) Frequency filter for time integration. Mon Wea Rev 100: 487–490

Baines PG, Hoinka KP (1985) Stratified flow over two-dimensional topography in fluid of infinite depth: A laboratory simulation. J Atmos Sci 42: 1614–1630

Blumen W (1965) A random model of momentum flux by mountain waves. Geofys Publ 26: 1–33

Booker JR, Bretherton RP (1967) The critical layer for internal gravity waves in a shear flow. J Fluid Mech 27: 513–539

Bretherton FP (1966) The time-dependent motion due to a cylinder moving in an unbounded rotating or stratified fluid. J. Fluid Mech 28: 545–570

Chun H-Y (1995) Enhanced responses of a stably stratified two-layer atmosphere to low-level heating. J Meteor Soc Japan 73: 685–696

Corby GA, Sawyer JS (1958) The airflow over a ridge: The effects of the upper boundary and high-level conditions. Quart J R Met Soc 84: 25–37

Deardorff JW (1971) On the magnitude of the subgrid scale eddy coefficient. J Comput Phys 7: 120–133

Deardorff JW (1972) Numerical investigation of neutral and unstable planetary boundary layers. J Atmos Sci 29: 91–115

Durran DR (1986) Another look at downslope windstorms. Part I: On the development of analogs to supercritical flow in an infinitely deep, continuously stratified fluid. J Atmos Sci 43: 2527–2543

Durran DR, Klemp JB (1982) The effects of moisture on trapped mountain lee waves. J Atmos Sci 39: 2490–2506

Eliassen A, Palm E (1960) On the transfer of energy in stationary mountain waves. Geofys Publ 22: 1–23

Gal-Chen T, Somerville RC (1975) On the use of a coordinate transformation for the solution of the Navier-Stokes equations. J Comp Phys 17: 209–228

Klemp JB, Durran DR (1983) An upper boundary condition permitting internal gravity wave radiation in numerical mesoscale models. Mon Wea Rev 111: 430–444

Klemp JB, Lilly DK (1975) The dynamics of wave-induced downslope winds. J Atmos Sci 32: 320–339

Klemp JB, Lilly DK (1978) Numerical simulation of hydrostatic mountain waves. J Atmos Sci 35: 78–107

Laprise RJ, Peltier WR (1989) The linear stability of nonlinear mountain waves: Implications for the understanding of severe downslope windstorms. J Atmos Sci 46: 545–564

Lilly DK (1962) On the numerical simulation of buoyant convection. Tellus 14: 148–172

Lilly DK, Zipser EJ (1972) The front range windstorm of 11 January 1972 – A meteorological narrative. Weatherwise 25: 56–63

Lin Y-L, Wang T-A (1996) (LW): Flow regimes and transient dynamics of two-dimensional stratified flow over an isolated mountain ridge. J Atmos Sci 53: 139–158

Lin Y-L, Wang T-A, Weglarz RP (1993) Interactions between gravity waves and cold air outflows in a stably stratified uniform flow. J Atmos Sci 50: 3790–3816

Long RR (1953) Some aspects of stratified fluids. I. A theoretical investigation. Tellus 5: 42–58

Miles JW, Huppert HE (1969) Lee waves in a stratified flow. Part 4: Perturbation approximations. J Fluid Mech 35: 497–525

Orlanski I (1976) A simple boundary condition for unbounded hyperbolic flow. J Comput Phys 21: 251–269

Peltier WR, Clark TL (1979) The evolution and stability of finite-amplitude mountain waves. Part II: Surface wave drag and severe downslope winds. J Atmos Sci 36: 1498–1529

Pierrehumbert RT, Wyman B (1985) Upstream effects of mesoscale mountains. J Atmos Sci 42: 977–1003

Rottman JW, Smith RB (1989) A laboratory model of severe downslope winds. Tellus 41A: 401–415

Queney P, Corby GA, Gerbier N, Koschmieder H, Zierep J (1960) The airflow over mountains. WMO Tech. Note No. 34: 135 pp (Available from Secretariat of WMO, Geneva, Switzerland)

Scinocca JF, Peltier WR (1993) The instability of Long's stationary solution and the evolution toward severe downslope windstorm flow. Part I: Nested grid numerical simulations. J Atmos Sci 50: 2245–2263

Scorer RS (1949) Theory of waves in the lee of mountains. Quart J R Met Soc 75: 41–56

Shapiro R (1970) Smoothing, filtering, and boundary effects. Rev Geophys Space Phys 8: 359–387

Smith RB (1979) The influence of mountains on the atmosphere. Adv in Geophys 21: 87–230

Smith RB (1986) Further development of a theory of lee cyclogenesis. J Atmos Sci 43: 1582–1602

Smith RB (1989) Hydrostatic airflow over mountains. Adv in Geophys 31: 1–41

Stein J (1992) Investigation of the regime diagram of hydrostatic flow over a mountain with a primitive equation model. Part I: Two-dimensional flows. Mon Wea Rev 120: 2962–2976

Wang T-A: Mechanisms of wave ducting and severe downslope windslope windstorms in a structured shear flow. Ph.D. dissertation, Department of Marine, Earth, and Atmospheric Sciences, North Carolina State University, Releigh North Carolina 218 pp

Wang T-A, Lin Y-L (1999a) Wave ducting in a stratified shear flow over a two-dimensional mountain. Part I: General linear criteria. J Atmos Sci 56: 412–436

Wang T-A, Lin Y-L (1999b) Wave ducting in a stratified shear flow over a two-dimensional mountain. Part II: Implications for the development of high-drag states for severe downslope windstorms. J Atmos Sci 56: 437–452

Wang T-A, Lin Y-L, Semazzi HFM, Janowitz GS (1996) Response of a stably stratified atmosphere to large-scale diabatic forcing with applications to wind patterns in Brazil and the Sahel. J Geophys Res 101: 7049–7073

Authors' addresses: Dr. T.A. Wang, Air Traffic Services Division Civil Aeronautics Administration CAA Building 340, Tun-Hwa North Road Taipei 10592 Taiwan; Dr. Y.-L. Lin, Department of Marine, Earth and Atmospheric Sciences North Carolina State University Raleigh, North Carolina 27695-8208, USA